nature communications

Article

https://doi.org/10.1038/s41467-024-50735-w

A region-confined PROTAC nanoplatform for spatiotemporally tunable protein degradation and enhanced cancer therapy

Received: 3 August 2023

Accepted: 17 July 2024

Published online: 04 August 2024

Check for updates

Jing Gao[1,2,3], Xingyu Jiang[4], Shumin Lei[5], Wenhao Cheng[1], Yi Lai[1], Min Li[1], Lei Yang[1], Peifeng Liu[6], Xiao-hua Chen[7], Min Huang[8], Haijun Yu[1,5] ✉, Huixiong Xu[2] ✉ & Zhiai Xu[4] ✉

The antitumor performance of PROteolysis-TArgeting Chimeras (PROTACs) is limited by its insufficient tumor specificity and poor pharmacokinetics. These disadvantages are further compounded by tumor heterogeneity, especially the presence of cancer stem-like cells, which drive tumor growth and relapse. Herein, we design a region-confined PROTAC nanoplatform that integrates both reactive oxygen species (ROS)-activatable and hypoxia-responsive PROTAC prodrugs for the precise manipulation of bromodomain and extra-terminal protein 4 expression and tumor eradication. These PROTAC nanoparticles selectively accumulate within and penetrate deep into tumors via response to matrix metalloproteinase-2. Photoactivity is then reactivated in response to the acidic intracellular milieu and the PROTAC is discharged due to the ROS generated via photodynamic therapy specifically within the normoxic microenvironment. Moreover, the latent hypoxia-responsive PROTAC prodrug is restored in hypoxic cancer stem-like cells overexpressing nitroreductase. Here, we show the ability of region-confined PROTAC nanoplatform to effectively degrade BRD4 in both normoxic and hypoxic environments, markedly hindering tumor progression in breast and head-neck tumor models.

Heterobifunctional PROteolysis-TArgeting Chimeras (PROTACs) have emerged as a potent tool for manipulating protein homeostasis, which are generally composed of a target molecule that bind to protein of interest (POI) and a ligand to E3 ubiquitin ligase, and the linker connecting the ligand and target molecule[1–3]. PROTACs bind both a POI and an E3 ubiquitin ligase by forming a ternary complex, resulting in ubiquitination and subsequent degradation of the POI through the ubiquitin-proteasome pathway[4–8]. Notably, PROTACs drive catalytic degradation, allowing efficient targeting of a disease-causing POI at minimal doses with the potential to counteract the acquired drug resistance[9–11]. Despite the above advantages of PROTACs, several barriers still hinder their clinical translation. For instance, PROTACs display inefficient tumor accumulation due to their suboptimal pharmacokinetics and systemic side effects due to on-target but off-tumor protein degradation[12]. To date, a series of tactics have been developed to ensure tumor-specific protein degradation, including

[1]State Key Laboratory of Chemical Biology & Center of Pharmaceutics, Shanghai Institute of Materia Medica, Chinese Academy of Sciences, Shanghai 201203, China. [2]Department of Ultrasound, Zhongshan Hospital, Institute of Ultrasound in Medicine and Engineering, Fudan University, Shanghai 200032, China. [3]Department of Medical Ultrasound and Center of Minimally Invasive Treatment for Tumor, Shanghai Tenth People's Hospital, School of Medicine, Tongji University, Shanghai 200072, China. [4]School of Chemistry and Molecular Engineering, East China Normal University, Shanghai 200241, China. [5]School of Chinese Materia Medica, Nanjing University of Chinese Medicine, Nanjing 210023, China. [6]State Key Laboratory of Systems Medicine for Cancer, Shanghai Cancer Institute, Renji Hospital, School of Medicine, Shanghai Jiao Tong University, Shanghai 200032, China. [7]State Key Laboratory of Drug Research, Shanghai Institute of Materia Medica, Chinese Academy of Sciences, Shanghai 201203, China. [8]Division of Antitumor Pharmacology, Shanghai Institute of Materia Medica, Chinese Academy of Sciences, Shanghai 201203, China. ✉e-mail: hjyu@simm.ac.cn; xuhuixiong@126.com; zaxu@chem.ecnu.edu.cn

ligand-modifying strategies (e.g., antibody-PROTAC[13], folate-PROTAC[14] and aptamer-PROTAC conjugates[15]), stimuli-responsive methods (e.g., photoliable PROTACs[16–18], radiation-triggered PROTACs[19], hypoxia-responsive PROTACs[20], enzyme-activatable PROTACs[21]) and nanosystem-based delivery approaches (e.g., encapsulation by polymers[22] and covalent conjugation with polymers[23,24]). Unfortunately, the heterogeneity and complexity of solid tumors often render individual treatments insufficient. Therefore, it is crucial for researchers to explore practical strategies to address tumor heterogeneity.

Tumor heterogeneity poses a significant challenge in cancer therapy and is characterized by the diverse phenotypic profiles of cells within a tumor, each displaying varied treatment sensitivities[25,26]. For example, cancer stem-like cells (CSCs), also known as tumor-initiating cells, are pivotal in tumorigenesis due to their self-renewal and metastatic properties and resistance to conventional chemotherapy and radiotherapy, posing a major challenge in malignant tumor therapy[27–30]. Consequently, the eradication of CSCs within tumor tissue is essential for successful tumor regression[31,32]. CSCs predominantly reside in hypoxic regions in the tumor and maintain low levels of intracellular reactive oxygen species (ROS), contributing to their self-renewal and stem-associated factor expression[33–35]. Accordingly, hypoxia-activatable therapeutics have been developed to specifically eradicate CSCs[36]. Unfortunately, solid tumors also have normoxic zones near blood vessels that remain untouched by hypoxia-responsive treatment, thus attenuating the overall therapeutic impact. Therefore, a coordinated approach targeting both CSCs and non-CSCs is vital for optimized cancer treatment.

In this work, we rationally design a region-confined PROTAC nanoplatform to degrade bromodomain and extraterminal (BET) protein 4 (BRD4) concurrently under both normoxic (in which common tumor cells are located) and hypoxic (in which CSCs are enriched) conditions. This unified PROTAC nanoplatform is unique and tailored to respond to distinct tumor microenvironments arising from the inherent tumor heterogeneity, ensuring holistic tumor cell elimination. We first synthesize the ROS-responsive PROTAC prodrug ARV771-TK by incorporating a thioketal (TK) group that responds to ROS into the BRD4 PROTAC (ARV771). The PROTAC prodrug ARV771-TK is then copolymerized with the acid-responsive 2-(diisopropylamino)ethyl methacrylate (DPA) monomer through reversible addition-fragmentation chain transfer (RAFT) polymerization. Using a similar method, we synthesize another polymer containing the photosensitizer pyropheophorbide a (PPa) and DPA monomers. Upon intravenous injection, the self-assembling PROTAC nanoparticles (PGDAT) selectively accumulate in tumor tissues through the enhanced permeability and retention (EPR) effect. Matrix metalloproteinase 2 (MMP-2), which is overexpressed in tumors, further enhances tumor targeting by removing the poly(ethylene glycol) (PEG) corona. In the acidic environment within tumor cells, the photoactivity of PPa is rejuvenated, facilitating abundant ROS generation upon 671 nm laser exposure. This ROS cascade cleaves the TK linkage, releasing the core ARV771 PROTAC to enable targeted BRD4 degradation. Specifically, BRD4 degradation and photodynamic therapy (PDT) can markedly eliminate normoxic tumor cells. To address hypoxic CSCs in oxygen-deprived tumor niches, we further design a hypoxia-responsive PROTAC prodrug by modifying ARV771 with a nitrobenzyl group (termed ARV771-Nb), which is then incorporated into the abovementioned PROTAC nanoparticles (PGDAT@N) (Fig. 1a). Additionally, the latent hypoxia-responsive PROTAC prodrug is restored in hypoxic cancer stem-like cells overexpressing nitroreductase (Fig. 1b). Overall this region-confined PROTAC nanoplatform shows effective degradation of BRD4 in both normoxic and hypoxic environments thereby hindering tumor progression in breast and head-neck tumor models.

Results

Engineering and characterization of ROS-activatable PROTAC nanoparticles

To synthesize the ROS-responsive PROTAC prodrug, we selected BRD4-targeted ARV771 as the model PROTAC. BRD4 is increasingly viewed as an influential antitumor target because it regulates gene transcription related to the cell cycle and apoptosis[37]. The hydroxyl group on the Von Hippel-Lindau disease (VHL) ligand of ARV771 was modified with a methacrylate group via a cleavable thioketal (TK) spacer. This resulted in the creation of the ROS-activatable ARV771 prodrug, named ARV771-TK (Fig. 2a). Under PDT, the TK spacer of ARV771-TK can be cleaved by ROS, releasing ARV771. This allows BRD4 degradation in normoxic regions with abundant ROS. Moreover, a ROS-insensitive ARV771-TK counterpart was synthesized by coupling methacrylate with ARV771 through an ethylene glycol spacer (namely, ARV771-Et). The successful synthesis of these ARV771 derivatives was validated through proton nuclear magnetic resonance (^{1}H-NMR) and mass spectrometry (MS) (Supplementary Figs. 1–6). High-performance liquid chromatography (HPLC) and liquid chromatography-mass spectrometry (LC-MS) spectra showed that ARV771 could be regenerated from ARV771-TK upon coincubation with PPa and irradiation by a 671 nm laser, indicating the ROS-responsive activity of the ARV771-TK prodrug (Fig. 2b, Supplementary Fig. 7). Furthermore, we performed western blot analysis to investigate the BRD4 degradation properties of both ARV771 and ARV771-TK. ARV771 efficiently degraded the POI with a half-maximal degradation concentration (DC_{50}) of 22 nM in MDA-MB-231 TNBC tumor cells in vitro (Fig. 2c, Supplementary Fig. 8a). In contrast, the PROTAC derivative ARV771-TK showed limited POI degradation capacity (Fig. 2d, Supplementary Fig. 8b), primarily due to the disrupted interaction between the E3 ligase VHL and ARV771-TK.

After the ROS-responsive prodrug ARV771-TK was successfully synthesized, our next goal was to create acid-activatable and ROS-responsive PROTAC nanoparticles (Fig. 2e). Moreover, to enhance the tumor-specific accumulation and cellular uptake of the PROTAC nanoparticles, we incorporated an MMP-2-cleavable heptapeptide, GPLGLAG (GG), into the PEG-based macromolecular chain transfer agent for MMP-2-triggered removal of the PEG shell[38]. The PROTAC nanoparticles were achieved through PEG-containing chain transfer agent-induced RAFT copolymerization of ARV771-TK and an acid-responsive DPA monomer (named PGDT) to respond to intracellular acidity (e.g., pH 5.5–6.5)[39]. In addition, to obtain polymers with the potential to be used for PDT, the amphiphilic $mPEG_{113}$-GG-*b*-P(DPA_{35}-*r*-$HEMA_7$) (PGDH) diblock copolymer was synthesized first through PEG-containing chain transfer agent-induced RAFT copolymerization of 2-hydroxyethyl methacrylate (HEMA) and DPA. Then, PPa was grafted onto the PGDH backbone via an esterification reaction between the carboxy group of PPa and the pendant hydroxyl group of the PGDH copolymer (termed PGDA)[40]. We also developed control molecules without the MMP-2-cleavable heptapeptide through a similar method (termed PDT and PDA). Furthermore, we synthesized a ROS-inert PROTAC polymer (namely, PGDE) based on ARV771-Et via a similar method. The authenticity of all synthesized polymers was validated using ^{1}H-NMR spectroscopy (Supplementary Figs. 9–19). Gel permeation chromatography (GPC) measurements indicated that the copolymers had narrowly distributed molecular weights (Supplementary Table 3). The ROS-responsive property of the PGDT polymer was examined by GPC analysis. The results showed a delay in the retention time of PGDT after irradiation with a 671 nm laser in the presence of PPa, suggesting that the molecular weight of PGDT decreased due to cleavage of the TK spacer and subsequent removal of ARV771 from the copolymer (Supplementary Fig. 20).

The PGDAT nanoparticles that resulted from the co-assembly of PGDT and PGDA (Supplementary Fig. 21) were characterized using dynamic light scattering (DLS) and transmission electron microscopy

https://doi.org/10.1038/s41467-024-50735-w

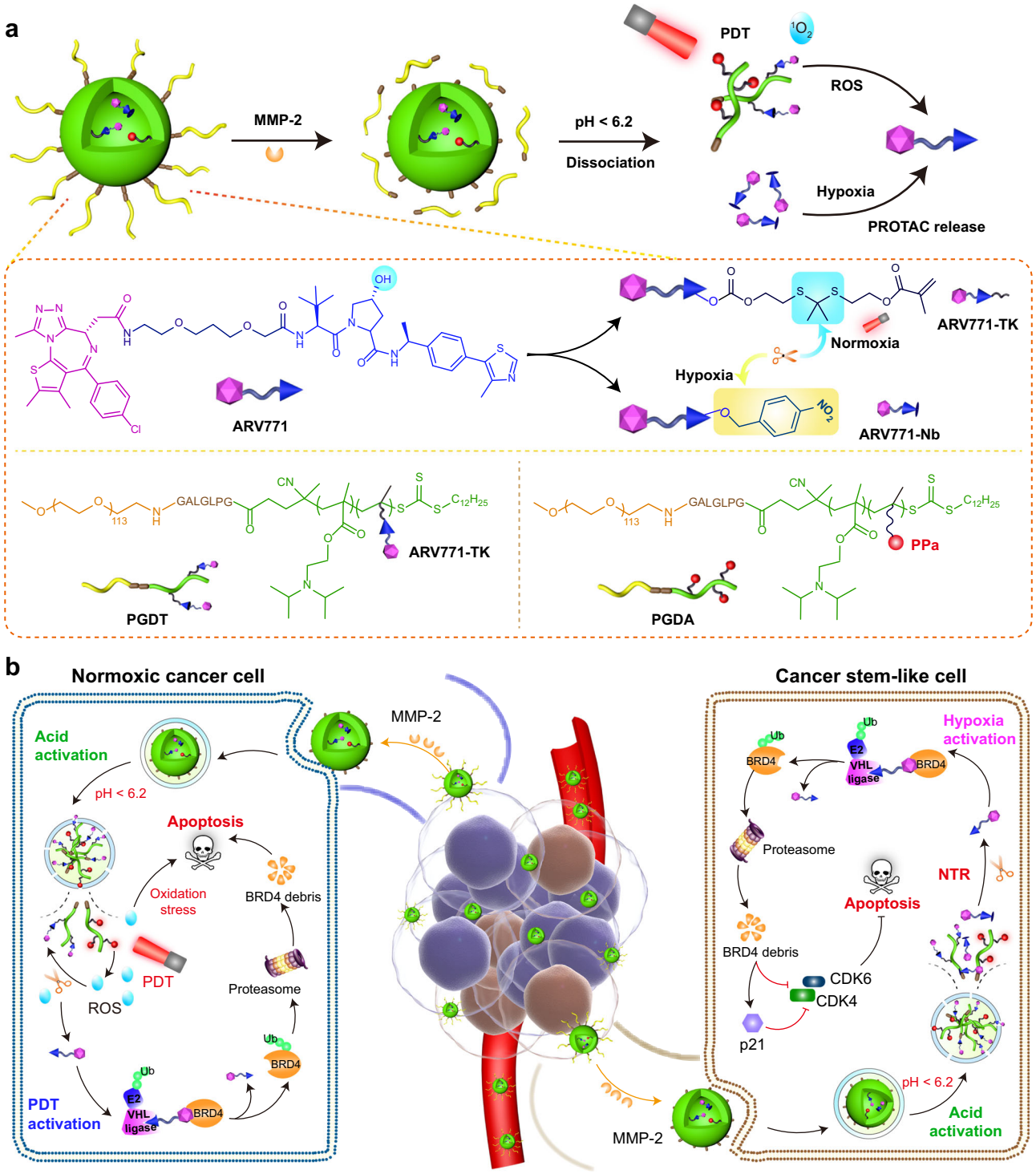

Fig. 1 | Schematic illustration of the region-confined PROTAC nanoplatform for spatiotemporally tunable protein degradation and combinatory cancer therapy. a Structure of the ROS/hypoxia dual-activatable PROTAC nanoparticle (PGDAT@N) and its responsive process to MMP-2 enzyme, intracellular acidic microenvironment, and PDT-based ROS or CSCs-relied hypoxia. **b** Cartoon illustration of the PGDAT@N nanoparticle eliminates tumor cells in normoxic and hypoxic areas simultaneously by self-complementary degrading BRD4 protein. PGDAT@N nanoparticle reaches tumor tissue after i.v. injection through EPR effect firstly, and MMP-2-induced PEG-deshielding enhances its accumulation and penetration at the tumor site. After internalized into tumor cells, PROTAC nanoparticle recovers its photoactivity due to acid-liable DPA groups caused dissociation of nanoparticle, and then affluent ROS in the normoxic region is generated under laser irradiation to release original PROTAC via cleaving the TK linkage. The BRD4 removal and PDT synergistically induce apoptosis of the normoxic tumor cells. Meanwhile, upon internalization by CSCs, hypoxia-activatable PROTAC derivate is divulged from the dissociated PGDAT@N nanoparticle, and then restored to parental PROTAC with nitroreductase (NTR) for sweeping tumor cells. BRD4 degradation can downregulate cell cycle proteins including cyclin-dependent kinase 4 (CDK4) and cyclin-dependent kinase 6 (CDK6), meanwhile upregulating cyclin-dependent kinase inhibitor 1 A (p21) to induce apoptosis of CSCs. The obliteration of both normoxic and hypoxic tumor cells with the region-confined PROTAC nanoplatform enable tumor regression efficiently.

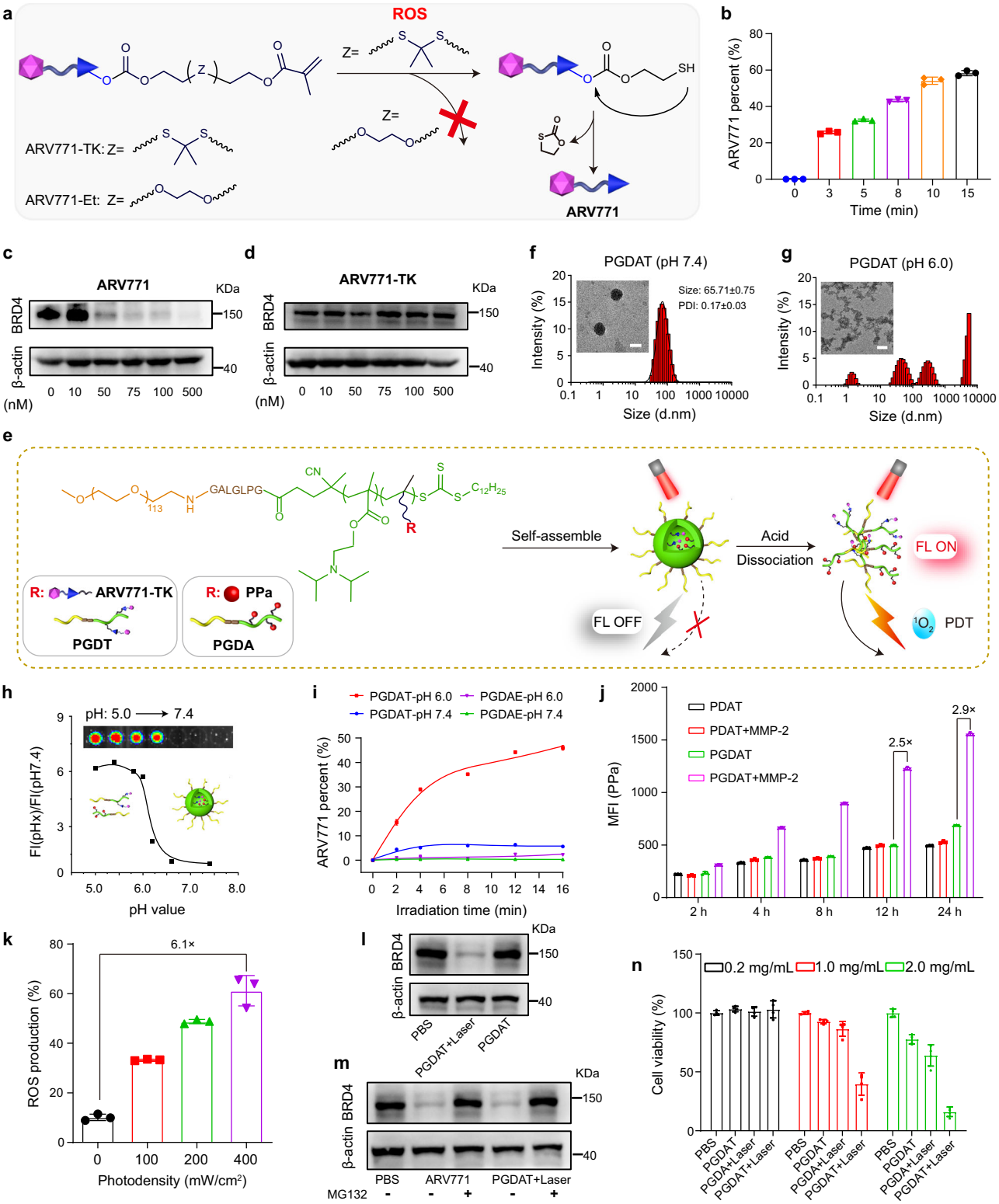

(TEM). These examinations revealed an average hydrodynamic diameter of ~65 nm, with the nanoparticles adopting a spherical morphology with a narrow particle size distribution (polydispersity index (PDI) < 0.2) at pH 7.4 (Fig. 2f). Conversely, at pH 6.0, which mimics acidic intracellular conditions, the PGDAT nanoparticles dissociated and formed amorphous aggregates due to the acid-triggered protonation of the DPA groups (Fig. 2g). The acid-activated behavior of the PGDAT nanoparticles was further illustrated by a fluorescence inversion experiment. Briefly, the fluorescence of PPa from the PGDAT nanoparticles was quenched under neutral conditions (pH 7.4) due to homofluorescence resonance energy transfer between the aggregated PPa molecules[41,42]. However, under acidic conditions (pH <6.2), which mimic the acidic microenvironment of the endosome (pH = 5.8–6.5), the fluorescence of PPa was 6.0-fold greater than that at pH 7.4, indicating the acid-induced disaggregation of the PGDAT nanoparticles (Fig. 2h). Moreover, fluorescence imaging of the PGDAT nanoparticles at different pH values using an IVIS fluorescence imaging system supported this observation, confirming the acid-induced

Fig. 2 | Synthesis and characterization of the ROS-activatable PROTAC nanoparticle. a Schematic illustration of ROS-induced restoration of ARV771 from ARV771-TK, but powerless of the counterpart ARV771-Et. **b** Release rate of ARV771 from ROS-activatable ARV771-TK after being mixed with PPa and irradiated by 671 nm laser with determined time ($n = 3$ independent experimental units). **c**, **d** Western blot analysis of ARV771 and ARV771-TK mediated BRD4 degradation in MDA-MB-231 cells post 24 h of co-incubation. **e** Schematic diagram of the self-assembly process and acid-activatable photoactivity capability of PGDAT nanoparticle. Representative DLS data and TEM images of the PGDAT nanoparticle at pH 7.4 (**f**) and pH 6.0 (**g**) condition (scale bar = 50 μm). **h** Acid-induced fluorescence recover profile of PGDAT nanoparticle, the fluorescence intensity was normalized to that determined at pH 7.4. Insert image was the PGDAT nanoparticle solutions at different pH values. **i** ROS-triggered ARV771 release from the PROTAC nanoparticles at the pH 7.4 and 6.0 with the different laser exposure time ($n = 3$ independent experimental units). **j** Flow cytometry evaluation of the cellular uptake of MMP-2-responsive PGDAT nanoparticle and MMP-2-inert PDAT nanoparticle by MDA-MB-231 cells after co-incubation with defined time in vitro (the nanoparticles were pretreated with/without MMP-2 of 0.2 mg/mL for 1 h) ($n = 3$ independent experimental cell lines). **k** Flow cytometric analysis of ROS production activity of PGDAT nanoparticle, DCFH-DA probe was joined into the tumor cells before laser irradiation with different photodensity ($n = 3$ independent experimental cell lines). **l** Western blot examination of BRD4 degradation of ROS-activatable PGDAT nanoparticle after 24 h co-incubation with MDA-MB-231 cell, the PGDAT nanoparticle was pretreated with 671 nm irradiation or not. **m** Western blot assay of MDA-MB-231 cells which were subjected to ARV771 and PGDAT nanoparticle with or without MG132 treatment (identical PROTAC concentration of 1.0 μM and MG132 concentration of 5.0 mM). **n** CCK-8 assay of MDA-MB-231 cell viability post different treatments ($n = 3$ independent experimental cell lines). All data are presented as mean ± SD.

disaggregation of the PGDAT nanoparticles. Additionally, serum stability is paramount for sustained in vivo circulation after injection[43]. DLS analyses demonstrated the robustness of the PGDAT nanoparticles, as they retained an average hydrodynamic diameter close to 65 nm even after 24 hours at various serum concentrations (Supplementary Fig. 22a).

Furthermore, the acid-activated PDT performance of the PGDAT nanoparticles was confirmed by evaluating ROS generation under neutral and acidic conditions with laser irradiation. The PGDAT nanoparticles were not photoactive at pH 7.4 regardless of the concentration of PPa and the photodensity. However, at pH 6.0, ROS generation significantly increased up to 7.3-fold greater than that at pH 7.4, which was attributed primarily to the acid-induced dissociation of the nanostructure (Supplementary Fig. 22b).

After demonstrating their acid-triggered photoactivity, we aimed to investigate the PROTAC release profile from the PGDAT nanoparticles under 671 nm laser irradiation. Using HPLC, ARV771 release was found to be minimal at pH 7.4. However, under acidic conditions (pH 6.0) and after treatment with a 671 nm laser, the release of ARV771 spiked in a time-dependent manner. On the other hand, the ROS-insensitive PGDAE nanoparticles displayed negligible ARV771 release, irrespective of pH (Fig. 2i). Collectively, these results emphasize the acid-induced photoactivity of the PGDAT nanoparticles, which lead to the generation of ROS under laser irradiation and subsequent activation of the ROS-responsive PROTAC through cleavage of the TK linkage. These results highlight the potential of the PGDAT nanoparticles as a precise PROTAC delivery system.

PROTAC nanoparticles performed MMP-2-enforced cellular uptake and ROS-triggered BRD4 degradation in vitro

Extending the circulation time of nanoparticles in the bloodstream is pivotal for targeted drug delivery, and PEGylation is commonly employed for this purpose[44]. However, a drawback of stably PEGylating nanomedicines is the consequent hindered cellular uptake and reduced penetration into deep tumor tissues[45,46]. To address these challenges, the strategy of PEG unshielding in response to a stimulus was employed in the PROTAC nanoparticle. Aim to demonstrate the MMP-2-mediated PEG unshell can enhance the celluar uptake of PROTAC nanoparticle, we pretreated both the PGDAT nanoparticle bearing the GG peptide spacer and its counterpart lacking the spacer (PDAT) with MMP-2 for 1 h to facilitate PEG shell cleavage. Subsequently, these nanoparticles were incubated with MDA-MB-231 human breast cancer cells for various durations. Flow cytometry analysis revealed a 2.9-fold greater intracellular fluorescence signal in the PGDAT group than in the PDAT group after 24 h of incubation (Fig. 2j). Confocal laser scanning microscopy (CLSM) analysis provided further evidence of increased intracellular uptake of the PGDAT nanoparticles with the GG peptide spacer after 12 h of coincubation (Supplementary Fig. 23). Taken together, these in vitro findings support the notion that MMP-2-induced PEG unshielding augments the internalization of PROTAC nanoparticles.

Upon their internalization into tumor cells, the photoactivity of the PROTAC nanoparticles recovered due to dissociation in the acidic intracellular microenvironment, promoting a surge in ROS generation under 671 nm laser irradiation, which in turn triggered the release of ARV771 for BRD4 degradation. Flow cytometry analysis revealed a substantial increase in the amount of ROS produced by the PROTAC nanoparticles, which peaked at 6.1-fold under 400 mW/cm^2 relative to that of the nonirradiated controls (Fig. 2k). Furthermore, CLSM images showed a similar fluorescence signal from PPa in PGDAT-treated tumor cells, while a notably brighter fluorescence signal from the ROS probe DCFH-DA was observed in the laser irradiation group (Supplementary Fig. 24). These findings confirmed the acid-induced ROS production capability of the PROTAC nanoparticles in vitro.

These promising results spurred further probing of the BRD4 degradation capabilities of the PGDAT nanoparticles via a western blot analysis. We observed a clear reduction in intracellular BRD4 expression when the nanoparticles were exposed to laser irradiation, whereas BRD4 expression remained largely unchanged in the absence of laser irradiation (Fig. 2l, Supplementary Fig. 25a). Furthermore, BRD4 degradation was pegged to the ubiquitin-proteasome pathway. This was evident from the fact that both the PROTAC molecule and PROTAC nanoparticles failed to induce protein degradation when they were paired with the proteasome inhibitor MG132 in MDA-MB-231 cells (Fig. 2m, Supplementary Fig. 25b). Notably, the CCK-8 assay revealed the synergistic cytotoxicity of BRD4 degradation and PDT. The PGDAT group exhibited weak tumor cell inhibition (~78% cell viability), while the PDT group (PGDA + laser) displayed moderate inhibition (~63% cell viability). Remarkably, coupling PGDAT with laser irradiation decreased the cell viability to a mere 16% at the same nanoparticle concentration of 2.0 mg/mL (Fig. 2n). Collectively, these findings underscore the ability of PROTAC nanoparticles to efficiently degrade the BRD4 protein and destroy normoxic tumor cells through the synergistic activity of PDT due to their ability to remove the PEG corona, be photoactive under acidic conditions, and release the PROTAC in response to ROS.

The PROTAC nanoparticles specifically promoted PDT and regenerated the BRD4 PROTAC at the tumor site in vivo

Next, we aimed to investigate the tumor-specific accumulation and penetration of the PEG-sheddable PROTAC nanoparticles (Fig. 3a). PGDAT nanoparticles (with the GG peptide) and MMP-2-inert PDAT analog nanoparticles were administered via intravenous (i.v.) injection to MDA-MB-231 tumor-bearing BALB/c nude mice at an identical PPa dose of 5.0 mg/kg when the tumor volume reached 150 mm^3. Photoacoustic imaging (PAI) in vivo revealed noticeable tumor distribution of both types of PROTAC nanoparticles over time owing to the EPR effect of the nanoparticles. Strikingly, elevated tumor accumulation

https://doi.org/10.1038/s41467-024-50735-w

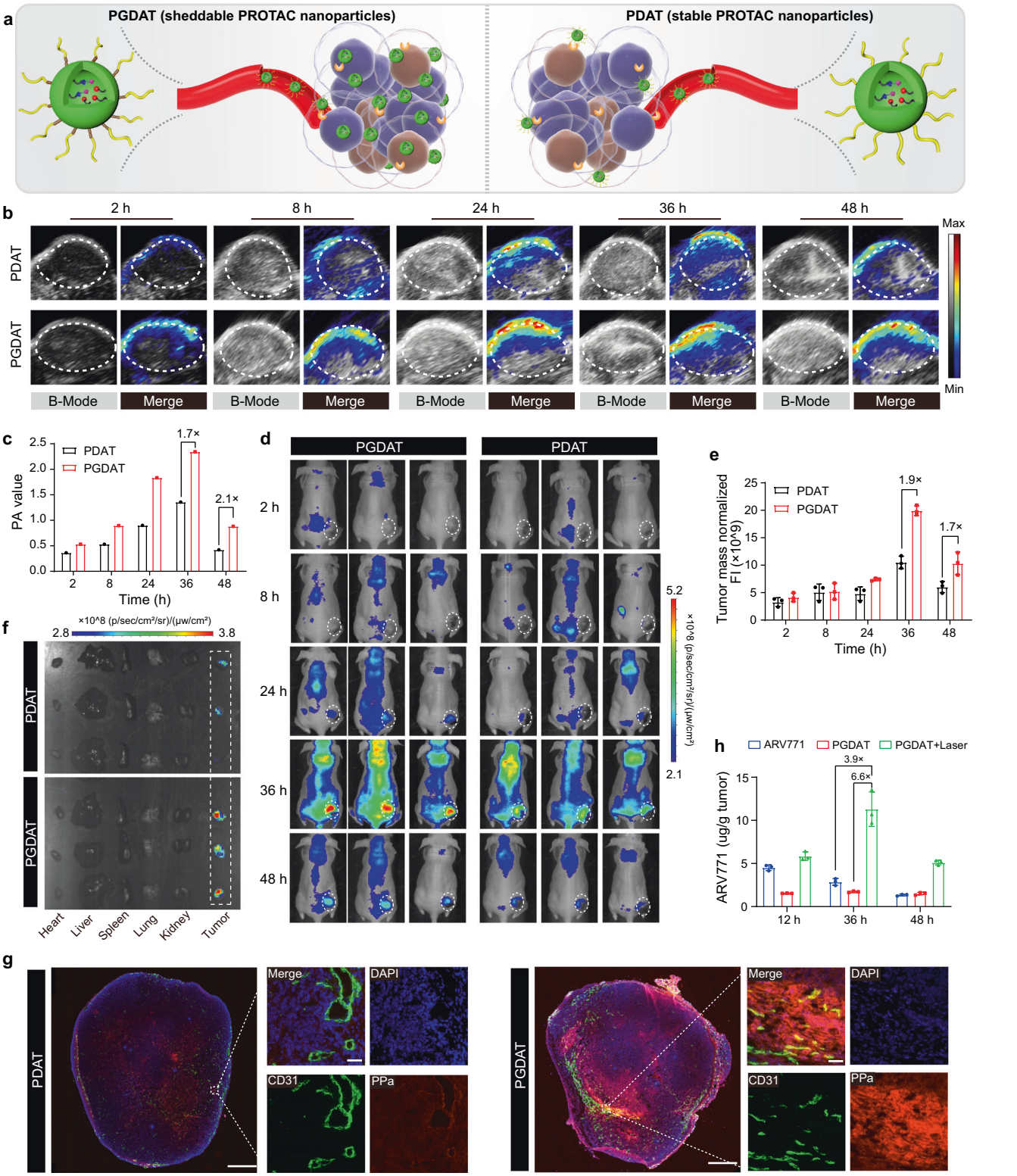

Fig. 3 | Stimuli-activatable PROTAC nanoparticle specifically accumulated and released free PROTAC at the tumor site in vivo. a Schematic diagram of sheddable PROTAC nanoparticles integrating MMP-2-lible GPLGLAG peptide spacer for enhanced tumor accumulation and penetration compared to the MMP-2-insensitive counterpart (without GPLGLAG peptide spacer). **b** Photoacoustic images (PAI) of PROTAC nanoparticle distribution in MDA-MB-231 tumor-bearing mouse model in vivo. **c** PA value of the tumor site ($n = 3$ mice). **d** Fluorescence imaging analysis of PGDAT (with MMP-2 responsive spacer) and PDAT (MMP-2-insensitive) nanoparticles distribution in MDA-MB-231 tumor-bearing nude mice. **e** Normalized fluorescence intensity of tumor site ($n = 3$ mice). **f** Ex-vivo fluorescence images of the harvested major organs (heart, liver, spleen, lung, kidney) and tumor tissues post 48 h treatment. **g** Ex-vivo CLSM images of tumor section post 48 h injection (left panel scale bar = 2.0 mm, right panel scale bar = 50 μm, the blue represents DAPI, the green represents CD31 and the red represents PPa). **h** HPLC evaluation of the intratumoral ARV771 distribution with different treatments (ARV771, PGDAT and PGDAT + laser groups with the identified ARV771 dose of 10 mg/kg) ($n = 3$ mice). All data are presented as mean ± SD.

and reduced blood clearance were observed in the MMP-2-sensitive PGDAT group, outperforming the PDAT control group at all examined intervals (Fig. 3b). Semiquantitative fluorescence evaluations at the tumor site revealed a 1.7-fold greater signal in the PGDAT group than in the PDAT control group 36 h after injection (Fig. 3c). Additionally, fluorescence imaging in vivo using IVIS corroborated these findings (Fig. 3d), showing a 1.9-fold greater tumor fluorescence signal for the PGDAT group at 36 h postinjection (Fig. 3e). Fluorescence imaging of the major organs (heart, liver, spleen, lung and kidney) and tumor tissues ex vivo at 48 h postinjection verified the tumor-specific accumulation of the PGDAT nanoparticles (Fig. 3f). A detailed CLSM image of the tumor sections further validated the highly diffuse distribution of the PGDAT nanoparticles throughout the tumor tissue, as these nanoparticles exhibited a stronger fluorescence signal than did the PDAT nanoparticles (Fig. 3g). In brief, the PAI, fluorescence imaging and CLSM results collectively illustrated that MMP-2-mediated removal of the PEG corona improved the tumor accumulation and penetration of the PROTAC nanoparticles in vivo.

Furthermore, we gauged the ROS generation capability of the PROTAC nanoparticles via CLSM analysis. At 36 h after i.v. injection of PROTAC nanoparticles into MDA-MB-231 tumor-bearing mice, intratumoral injection of the ROS probe DCFH-DA was performed. Subsequently, the tumor tissue was either irradiated with a 671 nm laser or not before being harvested for CLSM examination. In the absence of laser irradiation, a minimal green fluorescence signal indicative of DCF was observed. However, upon laser irradiation, a strong fluorescence signal was detected (Supplementary Fig. 26), indicating the ability of the PGDAT nanoparticles to generate ROS and potentially activate the ROS-responsive PROTAC. Therefore, the ARV771 distribution in vivo was then assessed through HPLC measurements. Here, the tumor accumulation of ARV771 was 6.6-fold and 3.9-fold greater in the group receiving laser-coupled PGDAT nanoparticles than in the group receiving PGDAT nanoparticles without laser irradiation and the free ARV771 group, respectively (Fig. 3h). These results consistently underscore the ROS-driven release of ARV771 from the PROTAC nanoparticles at the tumor site, leading to significantly greater accumulation of the PROTAC than that in the free ARV771 group. This finding suggests the heightened antitumor potential of such ROS-activatable PROTAC nanoparticles.

The ROS-activatable PROTAC nanoparticles moderately regressed tumor growth in vivo

The antitumor efficacy of the PROTAC nanoparticles was subsequently evaluated using MDA-MB-231 tumor-bearing BALB/c nude mice. The tumor-bearing mice were randomly grouped ($n = 6$) when the tumor volume reached ~100 mm^3 and intravenously injected with PBS, ARV771, PGDA nanoparticles or PGDAT nanoparticles at identical ARV771 doses of 10.0 mg/kg or PPa doses of 5.0 mg/kg. Thirty-six hours after injection, the mice in the PGDA + laser and PGDAT + laser groups were exposed to a 671 nm laser (Fig. 4a). The results showed negligible tumor inhibition in the free ARV771 and PGDAT groups compared to the PBS control group. The PDT group treated with PGDA + laser exhibited a moderate delay in tumor growth of approximately 50%. In contrast, the PGDAT + laser group displayed a remarkable tumor regression efficiency of ~80%, considerably extending the survival rate of the tumor-bearing mice (Fig. 4b–d). For instance, while all the mice in the PBS-treated group had died by Day 36 after the first treatment, ~67% of the mice in the PGDAT + laser group cohort survived. Moreover, one out of six tumors completely disappeared in the PGDAT + laser-treated mice, leading to a survival span of more than 80 days.

To explore the underlying mechanism of this pronounced tumor growth inhibition in the PGDAT + laser group, we performed hematoxylin and eosin (H&E) staining and TdT-mediated dUTP nick end labeling (TUNEL) staining on tumor sections. The results confirmed a significant increase in tumor cell apoptosis in the PGDAT + laser group (Fig. 4e, Supplementary Fig. 27). Furthermore, immunohistochemical staining and western blot analysis revealed substantial degradation of BRD4 at the tumor site in the PGDAT + laser group, which was in stark contrast to the minimal BRD4 degradation observed in the other treatment groups (Fig. 4f, g). For example, semiquantitative analysis of the western blot data indicated approximately 72% inhibition of the POI in the PGDAT + laser group compared to the PBS-treated group. In contrast, the PGDAT group without laser irradiation exhibited minimal BRD4 removal, indicating that the ROS generated by the PGDAT nanoparticles after laser irradiation effectively cleaved the TK linkage and successfully regenerated ARV771 (Fig. 4h). Moreover, throughout the monitoring period, the body weights of the mice in all the experimental groups were not significantly different from those of the mice in the PBS group (Supplementary Fig. 28a). Additionally, histopathological examinations of major organs (e.g., heart, liver, spleen, lung, and kidney) revealed no noticeable damage (Supplementary Fig. 28b), indicating good biosafety of the PROTAC nanoparticles in vivo.

Within the PGDAT + laser cohort, the tumors in four mice disappeared, highlighting the therapeutic efficacy of the nanoparticles. However, relapse occurred in three mice over the course of the monitoring period, culminating in only one surviving mouse (Fig. 4d). Therefore, we were inspired to reveal the underlying mechanism of this phenomenon. We speculated that the presence of lingering tumor cells was impervious to ROS-mediated elimination in hypoxic regions; therefore, attention shifted to the hypoxic area and self-hypoxic CSCs. CSCs, also referred to as tumor-initiating cells, are crucial factors contributing to tumor growth and metastasis in multiple malignancies[29].

We next investigated the changes in CSCs at the tumor sites in the MDA-MB-231 TNBC tumor-bearing mice following different treatments. Flow cytometry analysis revealed an increased population of CSCs in the laser irradiation groups (PGDA + laser and PGDAT + laser), which was 6.0-fold and 2.9-fold greater than that in the PBS-treated group, respectively (Fig. 4i). Consistent with these observations, the expression of stemness-associated proteins (e.g., NANOG, SRY-box transcription factor 2 (SOX2), and octamer-binding transcription factor 4 (OCT4)) revealed similar trends after flow cytometry evaluations (Fig. 4j–l). Immunohistochemical analysis further corroborated the above results (Fig. 4m–o). Taken together, these data suggest that the tumor recurrence observed in the PGDAT + laser group was primarily due to the persistence of breast CSCs.

PROTAC-driven BRD4 degradation reduced the stemness of CSCs in vitro

CSCs are predominantly found within hypoxic regions of tumors, as the hypoxic microenvironment is known to play a decisive role in CSC self-renewal[33]. Simultaneous eradication of non-CSCs and CSCs has therefore become a pivotal research focus for effectively suppressing tumor growth and preventing tumor relapse. In addition, PDT-induced ROS production relies on oxygen and may thus inadvertently cause oxygen deprivation in the environment[47]. Considering this, we next sought to investigate the latent changes in the hypoxia level and CSCs after the tumor was subjected to PDT. The hypoxic probe pimonidazole was utilized to examine the oxygen content in the tumor tissue, and an anti-CD133 antibody was used to label CSCs. We visualized laser irradiation-induced hypoxia through CLSM images of tumor sections from the PGDAT + laser group. Moreover, a concomitant increase in CSCs was also observed in the tumor tissue, especially in the hypoxic region (Fig. 5a). Immunohistochemical staining of hypoxia inducible factor (HIF), a hallmark of hypoxic tumor conditions, revealed enhanced HIF expression in the laser irradiation groups (PGDA + laser and PGDAT + laser), while the other groups (ARV771 and PGDAT) showed indiscriminate changes when compared with the PBS group (Fig. 5b).

https://doi.org/10.1038/s41467-024-50735-w

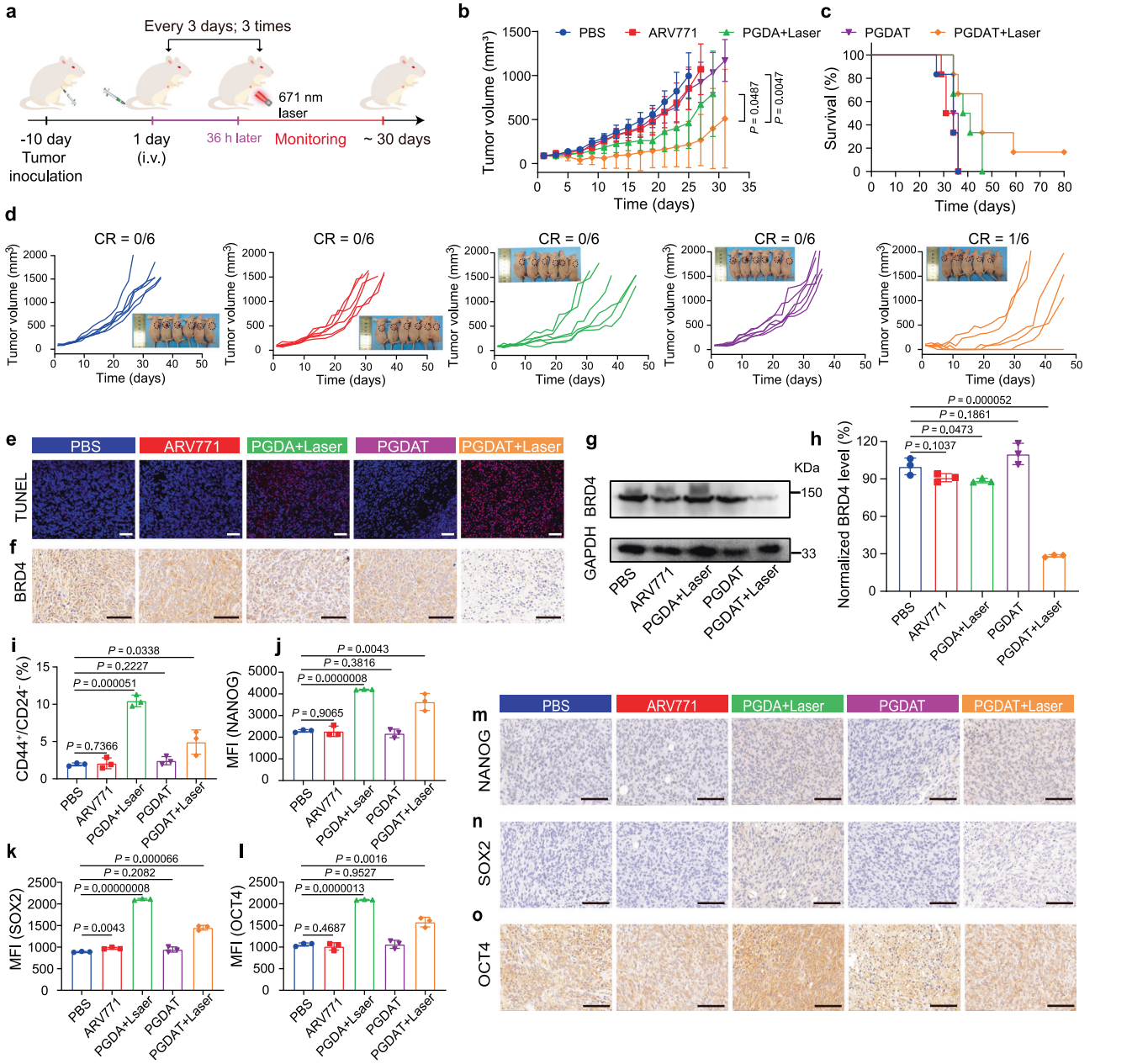

Fig. 4 | Antitumor performance of the ROS-activatable PROTAC nanoparticle in MDA-MB-231 breast tumor model in vivo. a Experimental schedule of the ROS-responsive PROTAC nanoparticles for antitumor study. **b** Tumor growth curves of the tumor-bearing mice subjected to different treatments ($n = 6$ mice), the statistical analysis was based on the two-sided unpaired *t*-test. **c** Survival plots of the tumor-bearing mice ($n = 6$ mice). **d** Individual tumor growth graph after being treated with various formulations, insert was photograph of tumor-bearing mice at 27-days post treatment ($n = 6$ mice). **e** TUNEL (blue: DAPI, red: apoptotic cells) staining of the tumor sections at end of various treatments (scale bar = 100 μm). **f** IHC examination of BRD4 expression in the tumor tissues (scale bar = 100 μm). **g** Western blot analysis and (**h**) semi-quantitation of BRD4 expression in the tumor lysates ($n = 3$ mice). Statistical analysis was performed by two-sided unpaired *t*-test. **i** Flow cytometric assay of intratumoral cancer stem-like cells ratio ($n = 3$ mice). Statistical analysis was performed by two-sided unpaired *t*-test. Flow cytometric analysis of the NANOG (**j**), SOX2 (**k**), OCT4 (**l**) expression in the tumor site upon various treatments ($n = 3$ mice). Statistical analysis was performed by two-sided unpaired *t*-test. IHC assay of the NANOG (**m**), SOX2 (**n**), OCT4 (**o**) expression of the tumor sections (scale bar = 100 μm). All data are presented as mean ± SD.

In addition to CSCs being enriched in the hypoxic region of tumors, CSCs in breast tumors reportedly exhibit lower levels of ROS than nontumorigenic cells[32]. To investigate this further, we enriched breast CSCs from MDA-MB-231 tumor cells through a serum-free suspension culture method[48,49]. The derived MDA-MB-231 tumor spheroids presented an obvious CD133-positive subpopulation, indicating the enrichment of cells with CSC-like characteristics (Supplementary Figs. 29a, b). Intriguingly, these tumor spheroids exhibited dramatically lower ROS levels (103.3-fold) than did common adherent MDA-MB-231 cells (Fig. 5c, d and Supplementary Fig. 29c). Briefly, hypoxia protects CSCs from the effects of the PGDA + laser and PGDAT + laser treatments, revealing the limited efficacy of PDT and BRD4 removal under hypoxic conditions.

We subsequently set out to find a viable course for CSC eradication. We previously demonstrated that BRD4 degradation efficiently inhibited non-CSC tumor cells. Therefore, this finding spurred an inquiry into the impact of BRD4 removal on CSCs. Both common MDA-MB-231 cells and CSCs were treated with ARV771 for 24 h, and transcriptomic analysis was conducted to examine the changes in gene expression following BRD4 degradation. In the comparison between

https://doi.org/10.1038/s41467-024-50735-w

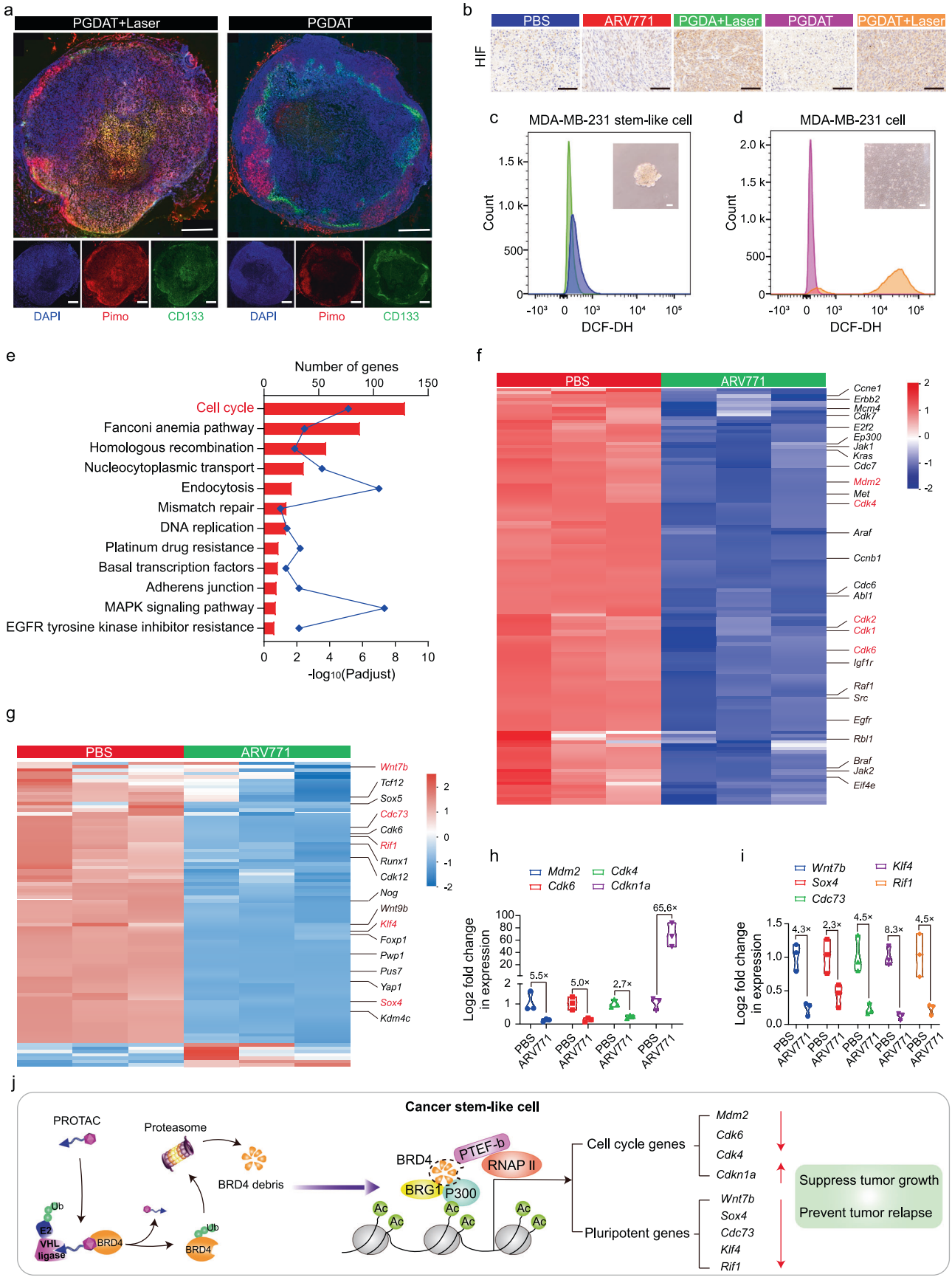

Fig. 5 | BRD4 degradation influenced the gene expression of cancer stem-like MDA-MB-231 tumor cells in vitro. a Immunofluorescence staining of tumor sections for hypoxia and cancer stem-like cells analysis (scale bar = 2.0 mm, the blue represents DAPI, the green represents CD133 and the red represents pimo). **b** IHC assay of HIF expression at tumor site after various treatments (scale bar = 100 μm). **c**, **d** Flow cytometry measurement of intracellular ROS level (insert: morphology image of different cells). **e**–**g** RNA-seq analysis of differential expression genes between MDA-MB-231 stem-like cells treated with PBS or ARV771 at the concentration of 1.0 μM for 24 h. **e** KEGG enrichment histogram of differentially expressed genes (statistical difference was calculated using two-sided Fisher's exact test, $n = 3$ independent experimental cell lines), **f** heatmap of differentially expressed genes associated with cell cycle and (**g**) cell stemness ($n = 3$ independent experimental cell lines, red and blue colors represent upregulated or downregulated genes respectively). Quantitative PCR assay of the (**h**) cell cycle- and (**i**) cell stemness-related RNA levels in MDA-MB-231 CSCs post 24 h incubation with 1.0 μM of ARV771 ($n = 3$ independent experimental cell lines). **j** Schematic illustration of PROTAC-induced BRD4 degradation and thus influence the downstream genes. All data are presented as mean ± SD.

ARV771-treated CSCs and untreated CSCs, a total of 9074 differentially expressed genes (DEGs) were identified, including 4997 upregulated genes and 4077 downregulated genes, using a threshold of an absolute fold change of > 2.0 and a p value < 0.05. A similar comparison between ARV771-treated and PBS-treated MDA-MB-231 cells revealed 7925 DEGs, with 3894 upregulated genes and 4013 downregulated genes (Supplementary Fig. 30). Kyoto Encyclopedia of Genes and Genomes (KEGG) pathway analysis further revealed that the downregulated DEGs in ARV771-treated CSCs were primarily related to the cell cycle, mismatch repair and the DNA replication signaling pathway (Fig. 5e). Similarly, the downregulated DEGs in ARV771-treated MDA-MB-231 cells were associated with the cell cycle, basal transcription factors and signaling pathways regulating the pluripotency of stem cells (Supplementary Fig. 31).

To understand the impact that the downregulated DEGs had on the growth of ARV771-treated CSCs, we investigated genes related to the cell cycle and the p53 signaling pathway (Fig. 5f). The results revealed that crucial genes involved in cell growth, including murine double minute 2 (*Mdm2*), cyclin-dependent kinase 4 (*Cdk4*), cyclin-dependent kinase 7 (*Cdk7*), cyclin-dependent kinase 1 (*Cdk1*), and cyclin-dependent kinase 6 (*Cdk6*), were significantly downregulated. A decreasing trend also emerged for certain proto-oncogenes (e.g., Kirsten rat sarcoma viral oncogene (*Kras*), c-mesenchymal-epithelial transition factor (*Met*), Abelson murine leukemia viral oncogene homolog 1 (*Abl1*), and murine leukemia viral oncogene homolog 1 (*Raf1*)). Similar patterns were observed in the analysis of DEGs from ARV771-treated MDA-MB-231 cells (Supplementary Fig. 32). Furthermore, a marked increase in cell apoptosis-related DEGs (e.g., those in the tumor necrosis factor (*Tnf*) receptor family and cyclin-dependent kinase inhibitor 1 A (*Cdkn1a*)) was detected in both CSCs and common MDA-MB-231 cells (Supplementary Fig. 33).

Moreover, it has been reported that BRD4 inhibition can suppress the expression of stemness-related genes in various malignant tumors[50]. We then focused on the changes in the expression of stemness-associated genes. Notably, several vital stemness-related DEGs were downregulated both in ARV771-treated CSCs and normal MDA-MB-231 cells (e.g., wingless-type MMTV integration site family member 7B (*Wnt7b*), Rap1 interacting factor 1 (*Rif1*), Kruppel-like factor 4 (*Klf4*), SRY-Box transcription factor 4 (*Sox4*) and cell division cycle 73 (*Cdc73*)) (Fig. 5g, Supplementary Fig. 32). Quantitative polymerase chain reaction (qPCR) analysis further confirmed the changes in the expression levels of crucial genes after MDA-MB-231 cells and CSCs were treated with ARV771. For instance, the expression of *Mdm2*, *Cdk4* and *Cdk6*, which are essential for cell proliferation, was obviously inhibited by 5.5-, 5.0- and 2.7-fold, respectively, compared with that in the PBS group when CSCs were treated with ARV771. Concurrently, the level of *Cdkn1a* (corresponding to the p21 protein), which can inhibit the function of *Cdk4* and *Cdk6*, was increased 65.6-fold compared to that in the PBS group after CSCs were treated with ARV771 (Fig. 5h). Comparable trends emerged in common MDA-MB-231 cells (Supplementary Fig. 34a). In addition, the expression of stemness-related genes (e.g., *Wnt7b*, *Sox4*, *Klf4*, *Rif1*, and *Cdc73*) decreased to different extents compared to that in the PBS group after CSCs and MDA-MB-231 cells were subjected to ARV771 treatment (Fig. 5i, Supplementary Fig. 34b). Taken together, these transcriptomic data revealed that BRD4 degradation in breast CSCs not only affects cell cycle genes, leading to cell cycle arrest and apoptosis, but also inhibits stemness-related genes, disturbing the self-renewal capacity of CSCs (Fig. 5j). These results indicated that ARV771 holds promise as a therapeutic avenue to curb CSCs, thus impeding tumor progression and preventing tumor recurrence.

The region-confined PROTAC nanoparticles inhibited tumor growth and recurrence via a BRD4 degradation both in vitro and in vivo

The hypoxic niche protects CSCs, but it can also serve as a target for their precise elimination. To this end, we devised a hypoxia-stimulating PROTAC prodrug for targeted CSC eradication. The hypoxia-responsive ARV771 derivative (ARV771-Nb) was generated by masking the hydroxyl group of the VHL ligand with 4-nitrobenzyl bromide[51], and the hypoxia-insensitive ARV771 derivative (ARV771-Ph) was prepared by introducing a benzyl group via a similar method (Fig. 6a, Supplementary Figs. 35–44). HPLC measurements revealed that ARV771 was fully restored from ARV771-Nb after incubation with 20 mM $Na_2S_2O_4$, whereas ARV771-Pb showed negligible changes (Fig. 6b, Supplementary Fig. 45), confirming the excellent reduction sensitivity of ARV771-Nb.

Furthermore, we investigated the impact of ARV771 and its hypoxia-liable derivative on protein expression in CSCs. Western blot analysis revealed significant BRD4 degradation in a dose-dependent manner for both ARV771 and ARV771-Nb, which had DC_{50} values of 73 nM and 95 nM, respectively, leading to the downregulation of CDK4 and CDK6 and the upregulation of p21 (Fig. 6c, d, Supplementary Fig. 46a, b). In contrast, the hypoxia-inert control, ARV771-Ph, had negligible effects on the expression of these proteins (Fig. 6e, Supplementary Fig. 46c).

Encouraged by the disruption of protein homeostasis caused by ARV771 and ARV771-Nb in CSCs, their ability to destroy CSCs was next investigated. A CCK-8 assay revealed that ARV771 and ARV771-Nb inhibited the viability of efficient CSCs with IC_{50} values of 0.42 μM and 0.57 μM, respectively, while ARV771-Ph showed significantly weaker activity (Supplementary Fig. 47). Moreover, ARV771 and ARV771-Nb impaired the ability of CSCs to form tumor spheroids, as evidenced by marked decreases in the number of tumor spheroids after 12 days of treatment with ARV771 and ARV771-Nb. For instance, there were approximately 90% and 83% fewer tumor spheroids after treatment with 1.0 μM ARV771 and 1.0 μM ARV771-Nb, respectively. In contrast, hypoxia-insensitive ARV771-Ph exhibited no significant difference ($p = 0.1515$) in the number of tumor spheroids compared to that in the PBS control group at different concentrations (Fig. 6f). Taken together, these data confirmed that ARV771-Nb could be activated within CSCs and selectively combat CSCs through its ability to induce BRD4 degradation.

With hypoxia-responsive ARV771-Nb in hand, we next developed a self-complementary PROTAC nanoparticle to simultaneously degrade the POI under both normoxia and hypoxia and thus eliminate both non-CSCs and CSCs. To this end, ARV771-Nb was encapsulated in ROS-activatable PROTAC nanoparticles, resulting in ROS/hypoxia-activatable PROTAC nanoparticles (termed PGDAT@N nanoparticles). The PGDAT@N nanoparticles had a uniform spherical shape with a

https://doi.org/10.1038/s41467-024-50735-w

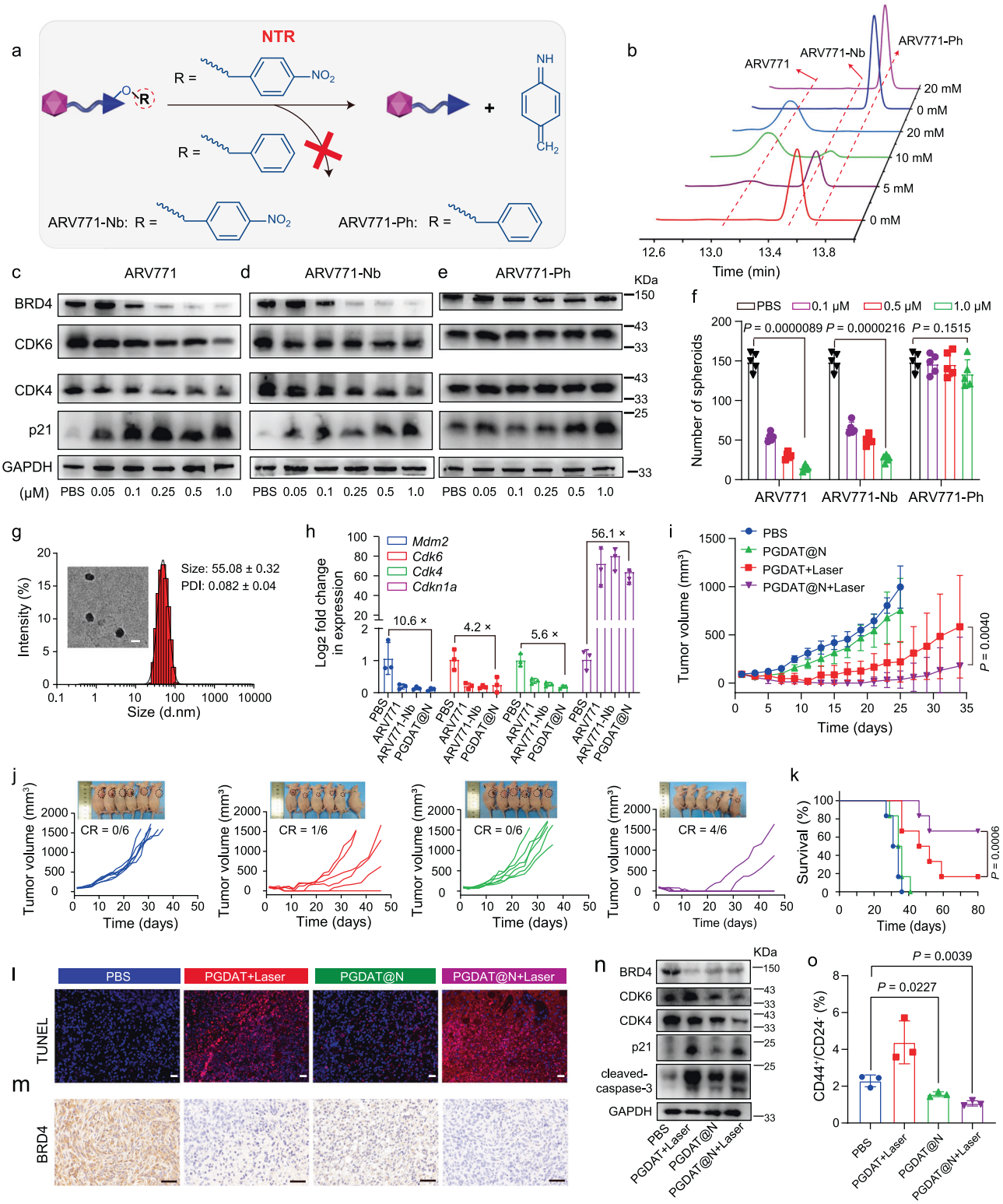

hydrodynamic diameter of ~55 nm and a narrow particle size distribution (PDI < 0.2) (Fig. 6g). HPLC analysis revealed the efficient release of ARV771 from the PGDAT@N nanoparticles upon 671 nm laser irradiation, which was attributed to its ROS-responsiveness, and subsequent restoration of ARV771 upon treatment with $Na_2S_2O_4$ (Supplementary Fig. 48), indicating its hypoxia-responsiveness[52]. These results confirmed the excellent ROS/hypoxia-activated performance of the PGDAT@N nanoparticles. Functionally, PGDAT@N closely mimicked the protein modulation capabilities of both ARV771-Nb and ARV771 in CSCs, as validated by q-PCR analysis (Fig. 6h, Supplementary Fig. 49a). Compared to free ARV771, the PGDAT@N nanoparticles and ARV771-Nb had compromised BRD4 degradation profiles in MDA-MB-231 cells in vitro, emphasizing the hypoxia-activatable activity of the PGDAT@N nanoparticles (Supplementary Figs. 49b, 50).

Next, we evaluated the tumor inhibition ability of the PGDAT@N nanoparticles using a CCK-8 assay in vitro, and exceptional tumor cell killing performance was observed after laser irradiation (Supplementary Fig. 51). Specifically, the PGDAT@N + laser group displayed

Fig. 6 | Synthesis of the region-confined PROTAC nanoparticle and its antitumor performance in MDA-MB-231 breast tumor model in vivo. a General view of hypoxia-responsive and hypoxia-insensitive ARV771 derivates. **b** Representative profiles of HPLC analysis on ARV771-Nb and ARV771-Ph treated with different concentrations of $Na_2S_2O_4$. Western blot assay of BRD4 expression and its downstream protein of CDK4, CDK6 and p21 in MDA-MB-231 stem-like cells with (**c**) ARV771, (**d**) ARV771-Nb and (**e**) ARV771-Ph treatment for 24 h. **f** Number of the tumor spheroids (diameter > 50 μm) after the MDA-MB-231 cells with various treatments for 12 days ($n = 5$ independent experimental cell lines). Statistical analysis was performed by two-sided unpaired *t*-test. **g** DLS data and TEM image of PGDAT@N nanoparticle (scale bar = 50 μm). **h** Quantitative PCR detection of RNA expression post 24 h treatment with different formulations in MDA-MB-231 stem-like cells ($n = 3$ independent experimental cell lines). **i** Averaged and (**j**) individual tumor growth profiles of tumor-bearing mice treated with diverse formulations (insert: mice image at 27 days of experimental period, $n = 6$ mice). Two-sided unpaired *t*-test was used in the statistical analysis. **k** Survival curves of tumor-bearing mice ($n = 6$ mice). Statistical analysis was performed by two-sided unpaired log-rank (Mantel-Cox) test. **l** TUNEL staining of the tumor sections (scale bar = 100 μm). **m** IHC analysis of BRD4 expression in the tumor sections (scale bar = 100 μm). **n** Western blot assay of PROTAC nanoparticle induced intratumoral BRD4 degradation and differential expression of its downstream proteins. **o** Flow cytometry examination of CSCs percentage in the tumor tissue post different treatments ($n = 3$ mice). Statistical analysis was achieved by two-side unpaired *t*-test. All data are presented as mean ± SD.

conspicuous tumor cell inhibition (~90%), outperforming its non-irradiated counterpart (~30%) and the PGDAT + laser group (~80%). This finding suggested that the assistance of hypoxia-responsive ARV771 for CSCs elimination can boost the tumor cell elimination activity of the PROTAC nanoplatform.

We then attempted to investigate the antitumor efficacy of the region-confined PROTAC nanoparticles in a xenograft MDA-MB-231 tumor model in vivo. Mice were randomly grouped when the tumor volume reached approximately 100 mm^3 and treated with PBS, PGDAT + laser, PGDAT@N or PGDAT@N + laser. Laser irradiation at 671 nm was applied to the tumor site 36 hours after intravenous injection of the PROTAC nanoparticles in the appropriate groups. The PGDAT@N + laser group exhibited a remarkable tumor regression rate of ~95%, with complete tumor disappearance in 4 out of the 6 mice and survival beyond 80 days. In contrast, in the PGDAT@N group, tumor growth was slightly inhibited by ~19%, and in the PGDAT + laser group, tumor growth was efficiently suppressed by ~80%; however, 3 mice experienced tumor relapse, resulting in only one mouse surviving for more than 80 days (Fig. 6i–k). H&E and TUNEL staining of the tumor sections showed notable tumor cell apoptosis in the PGDAT@N + laser group, while PGDAT + laser treatment displayed weaker tumor cell killing (Fig. 6l, Supplementary Fig. 52). These findings underscore that the elimination of CSCs or non-CSCs only by PGDAT@N or PGDAT + laser alone is not sufficient for effective antitumor activity. However, the simultaneous eradication of non-CSCs and CSCs in the PGDAT@N + laser group demonstrated superior performance in suppressing tumor growth and preventing recurrence. Furthermore, the mice displayed minimal loss of body weight and negligible histopathological damage to the major organs throughout the experimental period, suggesting the satisfactory biosafety of the PROTAC nanoparticles (Supplementary Fig. 53a, b).

To elucidate the mechanism underlying the antitumor effect of the PROTAC nanoparticles, BRD4 degradation in tumor tissue was evaluated through immunohistochemical analysis after tumor-bearing mice were subjected to different treatments. Compared with the other groups, the PGDAT@N + laser group exhibited more efficient suppression of BRD4 expression in the tumor tissue (Fig. 6m). Western blot analysis further confirmed notable BRD4 degradation in the PGDAT + laser group, with a 65% inhibition rate, and in the PGDAT@N + laser group, with 80% degradation, and BRD4 removal inhibited CDK4 and CDK6 expression while upregulating the expression of p21 (Fig. 6n, Supplementary Fig. 54). Upregulated p21 can further inhibit the activities of the CDK4 and CDK6 proteins, leading to the upregulation of cleaved caspase 3, which promotes tumor cell apoptosis.

The preeminent performance of PGDAT@N + laser in preventing tumor recurrence prompted a deeper exploration of its underlying mechanisms. Flow cytometry analysis revealed a significant decrease in the percentage of CSCs in the PGDAT@N + laser group compared to that in the PBS group (*P* value of 0.0039, Fig. 6o), which was mostly attributed to the effective inhibition of CSCs by hypoxia-activated ARV771-Nb. These results were further supported by the down-regulated expression of key CSC markers in the PGDAT@N + laser group (e.g., NANOG, OCT4 and SOX2) (Supplementary Figs. 55, 56). In summary, the unique design of the region-confined PROTAC nanoplatform ensures its activation in both normoxic and hypoxic areas, simultaneously eliminating non-CSCs and CSCs, leading to the highly efficient regression of tumor growth and prevention of tumor relapse.

Notably, the region-confined activation of the PROTAC nanoplatform was investigated using immunofluorescence to analyze BRD4 expression in a normoxic area, in which the expression of HIF was lower, and in a hypoxic area with high HIF expression. Combinatory treatment by ROS-responsive PGDAT + laser exhibited obvious BRD4 degradation in the normoxic region (low expression of HIF). However, the hypoxia-sensitive PGDAT@N displayed the opposite results. Notably, in the ROS/hypoxia-activatable PGDAT@N + laser group, marked BRD4 removal was observed under both normoxic and hypoxic conditions (Fig. 7a, Supplementary Fig. 57).

The region-confined activation of the PROTAC nanoplatform in vivo was further illustrated using immunofluorescence. Briefly, the PROTAC was replaced with the fluorescence probe hemicyanine (CY), and the ROS-labile CY prodrug (CY-TK) and hypoxia-triggering CY prodrug (CY-Nb) were also synthesized, as shown in Fig. 7b (Supplementary Figs. 58–65). The vanished fluorescence signal of CY was restored upon removal of the modified group from the hydroxy group in response to ROS/NTR[53]. The ability of these materials to respond to stimuli was demonstrated by HPLC and fluorescence spectroscopy (Supplementary Fig. 66). CY-TK was also conjugated to the same polymer (PGDH) to obtain a PGDC polymer that can coassemble with the PGDA polymer to obtain an ROS-liable nanoparticle (PGDAC), and CY-Nb was further encapsulated to obtain ROS/hypoxia-activatable PGDAC@N nanoparticles (Supplementary Fig. 67). A hypoxia probe, pimonidazole, was utilized to indicate hypoxia. After different treatments, the tumor tissues were collected from MDA-MB-231 tumor-bearing mice for immunofluorescence analysis. The PGDAC + laser group displayed an obvious fluorescence signal from CY in the non-hypoxic area because CY was regenerated due to the ROS-mediated cleavage of CY-TK. In contrast, the fluorescence signal of CY in the PGDAC@N group was mostly localized in the hypoxia zone, which was mostly attributed to the recovery of CY from CY-Nb in the hypoxia area. Notably, the ROS/hypoxia-responsive PGDAC@N + laser group exhibited visible CY fluorescence signals in both the normoxic and hypoxic regions (Fig. 7c, Supplementary Fig. 68). In summary, the ROS-triggered PROTAC could be activated under normoxia and the hypoxia-activatable PROTAC could be restored in the hypoxic area, resulting in the partial degradation of BRD4. Notably, the ROS/hypoxia-activatable nanoplatform was active in both environments and further degraded the target protein in a spatiotemporal manner (Fig. 7d).

The PROTAC nanoparticles inhibited tumor growth in the HNSCC tumor model

To validate the generalizability of the region-confined ROS/hypoxia-activatable PROTAC nanoplatform for cancer therapy, we further

https://doi.org/10.1038/s41467-024-50735-w

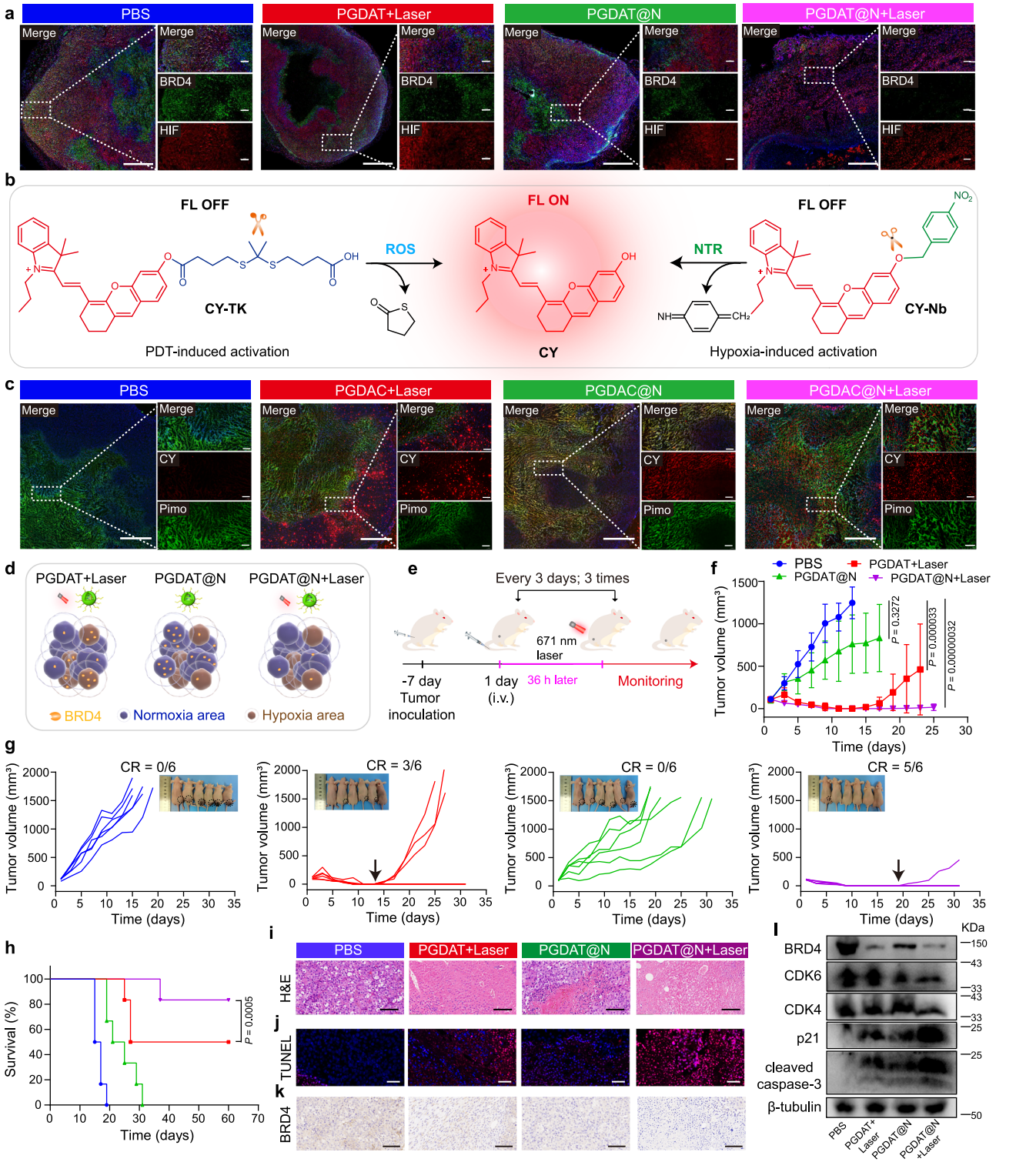

Fig. 7 | Region-confined activation of the PROTAC nanoparticle and its antitumor property in HN30 HNSCC tumor model in vivo. a IF staining of tumor sections for hypoxia (HIF) and BRD4 analysis after the tumor-bearing mice subjected to different treatments (left panel scale bar = 1.0 mm, right panel scale bar = 200 μm, the blue represents DAPI, the green represents BRD4 and the red represents HIF). **b** Schematic illustration of the ROS/NTR-triggered activation of CY from CY prodrugs. **c** Ex-vivo CLSM images of tumor sections post tumor-bearing mice subjected to various treatments for analysis of hypoxia (pimonidazole, pimo) and CY fluorescence (left panel scale bar = 1.0 mm, right panel scale bar = 200 μm, the blue represents DAPI, the green represents pimo and the red represents CY). **d** Cartoon illustration of region-confined activation of the nanoparticle and degradation of target protein BRD4. **e** Treatment schedule of the ROS/hypoxia-liable PROTAC nanoplatform antitumor study in HN30 tumor-bearing mice model. **f**–**h** PROTAC nanoparticle inhibited HN30 HNSCC tumor growth and relapse efficiently. Tumor growth curves (**f**) and individual tumor growth profiles (**g**) and survival plots (**h**) of the tumor-bearing mice upon treatment ($n = 6$ mice). Statistical analysis of **f** was performed by two-sided unpaired t-test. Statistical significance of **h** was calculated by survival curve comparison with Log-rank (Mantel-Cox) test. **i** H&E staining and **j** TUNEL (blue: DAPI, red: apoptotic cells) of tumor sections 15-days post-treatment (scale bar = 100 μm). **k** IHC analysis of BRD4 expression in the tumor tissues (scale bar = 100 μm). **l** Western blot assay of BRD4, CDK6, CDK4, p21, cleaved-caspase-3 expression of HN30 tumor tissues post tumor-bearing mice subjected to various treatments. All data are presented as mean ± SD.

investigated its antitumor efficacy in a mouse model of HN30 HNSCC tumors. Initially, we demonstrated the BRD4 degradation capability of ARV771 in HN30 tumor cells (Supplementary Fig. 69). Then, HN30 tumor-bearing mice were subjected to treatments as delineated in Fig. 7e. The group treated with PGDAT@N + laser exhibited remarkable tumor regression, with complete tumor eradication in 5 of the 6 mice, and survival beyond 60 days (Fig. 7f–h). The group receiving only PGDAT@N showed a moderate tumor growth inhibition rate of ~34% on Day 17 of monitoring. Conversely, the PGDAT + laser group exhibited an efficient tumor suppression rate of ~ 88%, with 3 cases of tumor recurrence, resulting in only 2 mice surviving beyond 60 days. H&E and TUNEL staining of the tumor sections showed notable tumor cell apoptosis in the PGDAT@N + laser group, while the PGDAT@N and PGDAT + laser groups displayed weaker tumor cell killing abilities (Fig. 7i, j).

The antitumor mechanism of the PROTAC nanoparticles was further elucidated through immunohistochemical analysis of the tumor tissues after treatments. Compared to the other groups, the PGDAT@N + laser group exhibited more efficient BRD4 degradation in the tumor tissue (Fig. 7k). Western blot assays further demonstrated an 85% BRD4 degradation rate in the PGDAT@N + laser group, resulting in notable inhibition of CDK6 (~60%) and CDK4 (~50%) (Fig. 7l, Supplementary Fig. 70). Additionally, the protein expression levels of p21 and cleaved caspase 3 were clearly upregulated 5.0-fold and 4.3-fold, respectively, compared to those in the PBS group, indicating satisfactory tumor cell apoptosis (Supplementary Fig. 70). Therefore, the multifunctional PROTAC nanoparticles simultaneously targeted proteins in both normoxic and hypoxic tumor regions, demonstrating promising antitumor therapeutic efficacy in two different tumor-bearing mouse models.

Discussion

PROTACs hold promise for treating refractory cancers due to their ability to efficiently degrade onco-proteins and circumvent drug resistance. Nonetheless, the clinical application of PROTACs is hindered by insufficient tumor-specific delivery and systematic adverse effects caused by the on-target but off-tumor degradation of the target protein. Therefore, we were inspired to develop a distinctive PROTAC technology for highly efficient and spatiotemporally tunable protein regulation with minimal side effects. It is well-documented that tumor heterogeneity contributes to inconsistent treatment responses, especially in the presence of CSCs, which compromises tumor suppression and induces tumor relapse. To this end, we developed a region-confined PROTAC nanoplatform that attuned to diverse tumor microenvironments for spatiotemporally-tunable degradation of the oncoprotein BRD4 in normoxic and hypoxic areas of tumors.

This pioneering region-confined PROTAC nanoplatform builds upon the foundational PROTAC molecule ARV771 but responds to distinct tumor microenvironments caused by the inherent heterogeneity of the tumor, eliminating tumor cells with different features simultaneously. The ROS/hypoxia-activatable PROTAC nanoparticles showed enhanced tumor accumulation and penetration via MMP-2-induced removal of the PEG corona and restored photoactivity owing to the acidic intracellular microenvironment, which caused dissociation of the PGDAT@N nanoparticles. Upon exposure to 671 nm laser irradiation, large amounts of ROS were generated in the oxygen-enriched region to cleave the TK bond, releasing the original PROTAC to degrade BRD4 and destroy tumor cells. Moreover, hypoxia-activatable ARV771-Nb recovered its ability to remove the POI, especially in oxygen-depleted regions and hypoxic CSCs. Bioinformatics analysis of the clinical database further validated that MMP-2 is overexpressed in a broad spectrum of solid tumors in human patients (Supplementary Fig. 71), which can serve as a general stimulus to induce dePEGylation of the PROTAC nanoparticles and facilitate their accumulation at the tumor site, thus overcome tumor heterogeneity. To further combat tumor heterogeneity and promote nanoparticle distribution at the tumor site, other kinds of endogenous stimuli, for example, fibroblast activation protein-α (FAP) widely up-regulated in various solid tumors can also be exploited for the dePEGylation strategy to promote tumor accumulation of nanomedicine.

In summary, we reported a region-confined PROTAC nanoplatform for spatiotemporally tunable protein degradation and enhanced cancer therapy in different tumor models that can be activated by multiple endogenous and exogenous stimuli, including intratumoral MMP-2, intracellular acidity and PDT-induced ROS in the normoxic region or NTR in the hypoxic region. Compared to conventional PROTACs, the PROTAC nanoparticles described in this study offer several advantages. First, the PROTAC nanoparticles show enhanced accumulation and penetration at the tumor site for tumor-targeted PROTAC delivery via extracellular MMP-2-triggered deshielding of the PEG corona. Second, the stimuli-sensitive PROTAC nanoplatform specifically promoted PDT at the tumor site by responding to the acidic or normoxic intracellular microenvironment. Given the advantage of PDT-triggered spatiotemporally confined ROS-responsive PROTAC activation, BRD4 degradation occurs only within the tumor cells of the normoxic region, minimizing adverse effects. Third, the PROTAC nanoplatform considers tumor heterogeneity, allowing the hypoxia-liable PROTAC to be activated in the hypoxic region and subsequently degrading BRD4 in CSCs. More importantly, in comparison to a single regulatory strategy involving PGDAT or PGDAT@N nanoparticles, the ROS/hypoxia-activatable PGDAT@N nanoplatform enables complete eradication of tumor cells, including non-CSCs and tough CSCs. Tumors disappeared in 4/6 MDA-MB-231 TNBC tumor-bearing mice and 5/6 HN30 tumor-bearing mice treated with PGDAT@N + laser, but tumors disappeared in only one or two mice after PGDAT + laser treatment. Despite insufficient tissue penetration depth has been a challenge for clinical application of phototherapy, recent advance of fiber optics and endoscopic lasers can guide laser intervention deep into the body, largely expanding the application of photodynamic therapy. In addition, with an in-depth understanding of various tumor biomarkers and advancements in exogenous stimuli, the PROTAC nanoparticle design can be further generalized to modulate protein homeostasis by integrating other endogenous biomarkers (e.g., glutathione, esterase, cathepsin B, redox) and exogenous stimuli (e.g., X-ray, ultrasound, magnetic and electric fields). Overall, the region-confined PROTAC nanoplatform described herein not only represents a pioneering combinational therapeutic modality but also extends the horizons for PROTAC-driven cancer therapy.

Methods

The research complies with all relevant ethical regulations of the Shanghai Institute of Materia Medica, Chinese Academy of Sciences. The Sequences of PCR primers are provided in the Supplementary Table 2. The company and catalog numbers of commercial reagents are provided in the Materials section of Supplementary Information.

Cell lines and animals

MDA-MB-231 human breast cancer cell line (CRM-HTB-26) and HN30 head and neck squamous cell carcinoma (TCP-1012) were obtained from ATCC (Shanghai, China). These cell lines were authenticated using STR analysis and the last authentication testing time of MDA-MB-231 is 2/4/2024, the HN30 is 20/12/2023. All cell lines were tested negative for mycoplasma contamination examined by Hoechst DNA staining and qPCR-based assay. The cells were maintained in DMEM medium with 10% FBS (V/V), penicillin G sodium and streptomycin sulfate (100 U/mL), and incubated at 37 °C with 5% CO_2 supply. All cellular experiments in vitro were conducted during the logarithmic phase of cell growth in vitro.

To enrich cancer stem-like cells, a serum-free suspension culture method was applied[48,49]. Briefly, MDA-MB-231 cells were cultured in

6-well ultralow attachment plate with culture medium comprised DMEM/F-12 with 1× B27 supplement, human epidermal growth factor (20 ng/mL), human basic fibroblast growth factor (20 ng/mL), penicillin and streptomycin (100 U/mL) in the tri-gas incubator (Sanyo, MCO-5M) under an atmosphere consisting of 1% O_2 and 5% CO_2. After cultured for 8–12 days, the formed tumor spheroids were harvested for further using. MDA-MB-231 cells and MDA-MB-231 stem-like cells were stained with anti-CD133 antibody as the manufacturers' protocol and analyzed via flow cytometry.

BALB/c nude mice (female, 4-5 weeks old, 18–20 g) were purchased from Shanghai Experimental Animal Center (Shanghai, China). The animals were housed under SPF condition in groups of 4–5 mice per cage, and maintained at a temperature of ~25 °C in a humidity-controlled environment with a 12 h light/dark cycle, and with free access to standard food and water. All experimental procedures involving animals were conducted in strict adherence to the guidelines of Institutional Animal Care and Use Committee (IACUC) of Shanghai Institute of Material Medica, Chinese Academy of Sciences. The maximal tumor size was not exceeded 2000 mm^3 during the experimental process.

The activation of ARV771-TK

ARV771-TK (50 μg) and PPa (50 μg) were dissolved in 1 mL of methanol, irradiated by 671 nm laser (400 mW/cm^2) for pre-determined time duration, and then the ARV771 release profile was examined by high performance liquid chromatography measurement (mobile phase: A: MeOH, C: H_2O with 0.1% TFA; flow rate: 1.0 mL/min; column temperature: 30 °C, UV: 254 nm, elute gradient: 0-10 min, from 5% A to 95% A; 15-20 min, from 95% A to 5% A).

Western blot assay

To assess the efficacy of PROTAC-mediated protein degradation in vitro, MDA-MB-231 cells or MDA-MB-231 stem-like cells were treated with ARV771, its derivatives or PROTAC nanoparticles. The cells were then harvested and lysed in RIPA lysis buffer (50 mM Tris-HCl pH7.4, 150 nM NaCl, 1% NP-40, 0.1% SDS) containing 1 mM of phenylmethanesulfonylfluoride (PMSF). The mixture was centrifugation at 12,000 g at 4 °C for 15 min, and the supernatant was then collected as the protein lysate. The protein lysate was quantitated by BCA protein quantification kit, and then denatured at 100 °C including 20% (v/v) loading buffer. The protein lysate was resolved by SDS-polyacrylamide gel electrophoresis (SDS-PAGE). The gel was then blotted onto PVDF membrane (Merck Millipore) and blocked through 5% bovine serum albumin (BSA) buffer for 2 h at room temperature. Afterward, the membrane was incubated with the indicated primary antibody (1:1000) at 4 °C overnight, subsequently, incubated with corresponding secondary antibody (1:5000) in 5% BSA for 1 h under room temperature. Finally, the membrane was imaged by Tanon imaging system.

Preparation of the PROTAC nanoparticle

Briefly, 2.0 mg of $mPEG_{113}$-GALGLPG-*b*-P(DPA_{36}-*r*-ARV771-TK_2) and 1.0 mg of $mPEG_{113}$-GALGLPG-*b*-P(DPA_{35}-*r*-$HEMA_7$-PPa_4) diblock copolymers were dissolved in 100 μL of DMF. The above solution is added dropwise into 1.0 mL of DI water under ultrasonication, aiding the nanoparticle formation. The organic solvent is than removed through dialysis against DI water, resulting in the desired PROTAC nanoparticle, namely PGDAT nanoparticle. The other PROTAC nanoparticles were synthesized using a consistent method named according to their components:

MMP-2-insensitive PDAT nanoparticle: $mPEG_{113}$-*b*-P(DPA_{35}-*r*-ARV771-TK_2) + $mPEG_{113}$-*b*-P(DPA_{39}-*r*-$HEMA_7$-PPa_4);

Reactive oxygen species (ROS)-insensitive PGDAE nanoparticle: $mPEG_{113}$-GALGLPG-*b*-P(DPA_{35}-*r*-$HEMA_7$-PPa_4) + $mPEG_{113}$-GALGLPG-*b*-P(DPA_{36}-*r*-ARV771-Et_2).

To prepare the ROS/hypoxia-activatable PROTAC nanoparticle (PGDAT@N nanoparticle), 1.0 mg of $mPEG_{113}$-GALGLPG-*b*-P(DPA_{36}-*r*-ARV771-TK_2), 1.0 mg of $mPEG_{113}$-GALGLPG-*b*-P(DPA_{35}-*r*-$HEMA_7$-PPa_4) and 100 μg of ARV771-Nb were dissolved in 100 μL of DMF. The mixture was then added dropwise into 1 mL of DI water while maintaining an ice bath accompanied by ultrasonication. Finally, the solvent was removed via dialysis against DI water.

Physiochemical characterisation of the PROTAC nanoparticles

Hydrodynamic diameters and morphology of all the nanoparticles were examined by DLS (Zetasizer Nano ZS90, Malvern Instrument, UK) and transmission electron microscope (TEM, Talos L120C, USA, 120 KV) examination, respectively. The fluorescence signal intensity of the PGDAT nanoparticle in different pH buffer was analyzed through mocroplate reader (Perkin Elmer Enspire, USA). Additionally, fluorescence imaging was conducted with the IVIS imaging system (Xenogen, Alameda, CA).

Photoactivity of the PGDAT nanoparticle

To evaluate the photoactivity of the PROTAC nanoparticle, the PGDAT nanoparticle was added into a buffer solution at pH 6.0 or pH 7.4 (the final identified PPa concentration is 2.5 or 5.0 or 10 μM), then left to stand for 30 min. The single oxygen sensor green (SOSG, 5.0 μM) was added into the suspension. The entire sample was then subjected to irradiation using a 671 nm laser at different photodensities (e.g., 100, 200 or 400 mW/cm^2) for 1 min. To measure the resulting fluorescence intensity of SOSG, a microplate reader (Perkin Elmer Enspire, USA) was utilized.

PROTAC release profile of the PROTAC nanoparticles

The ROS-sensitive PGDAT and ROS-inert PGDAE nanoparticle in pH 6.0 or pH 7.4 buffer solution were irradiated by 671 nm laser for predetetmined time (e.g., 0, 2, 4, 8, 12, 16 min). Then, each solution was mixed with methanol (1:1, v-v) and further analyzed through HPLC examination to give the ARV771 concentration of the mixture.

Cellular uptake profile of the PROTAC nanoparticle in vitro

Various PROTAC nanopartilces with identified PPa concentration of 5 μM were incubated with MDA-MB-231 cells cultured in 12-well culture plate. At the predetermined time durations (e.g., 2, 4, 8, 12, 24 h), the intracellular fluorescence intensity was measured through flow cytometry (BD FACS Fortessa, BD, USA). At the desired time duration of 12 h, the intracellular distribution of the PROTAC nanoparticle was examined by CLSM examination.

Cytotoxicity assay

MDA-MB-231 cells or CSCs were incubated in a 96-well tissue-culture plate and treated with PROTAC, PROTAC derivantstives, or PROTAC nanoparticles. Then, cell viability was determined using the CCK-8 assay in accordance with the manufacturers' instructions.

Photoactivity of PROTAC nanoparticle in vitro and in vivo

MDA-MB-231 cells were incubated with the PGDAT nanoparticle in a 24-well culture plate for 12 h. Upon 20 min incubatation with DCFH-DA (10 μM), the cells were exposed to 671 nm laser for 1 min at different photodensities (e.g., 100, 200, 400 mW/cm^2). The resulting intracellular fluorescence intensity of DCF was investigated using flow cytometry and CLSM assay.

An orthotopic MDA-MB-231 tumor model was established by subcutaneously injecting 5.0×10^6 MDA-MB-231 tumor cells into the second mammary fat pad of BALB/c nude mice. Once the tumor volume reached ~150 mm^3, the mice were intravenously injected with PGDAT nanoparticle. DCFH-DA probe was intratumoral injected into the tumor tissues 36 h post nanoparticle injection, and then the tumors were subjected to 671 nm laser irradiation for 5 min at 400 mW/cm^2. Afterward, the tumor tissues were harvested for further section and stained with DAPI, and examined by CLSM.

Biodistribution of the nanoparticles in vivo

MDA-MB-231 subcutaneous tumor-bearing mouse model was established through subcutaneously injecting 100 μL of cell suspension (5×10^6 cells) into the right back the BALB/c nude mice. Once the tumor volume was reached about 150 mm^3, the mice were randomly grouped. Subsequently, MMP-2-liable PGDAT or MMP-2-insensitive PDAT nanoparticles were intravenously (i.v.) injected at the identified PPa dose of 5.0 mg/kg. Photoacoustic (PA) imaging were performed at the pre-determined time points (Vevo® LAZR-X). Besides, fluorescence imaging of the mice were recorded using IVIS system (Xenogen, Alameda, CA). The mice were sacrificed 48 h post treatment, and the major organs (e.g., heart, liver, spleen, lung and kidney) along with tumor tissues were harvested and subjected to fluorescence imaging. Furthermore, the tumor tissues were fixed, sectioned, and stained with DAPI and anti-CD31 antibody for further analysis using CLSM.

Antitumor study in vivo

To evaluate the antitumor performance of the ROS-responsive PROTAC nanoparticle in vivo, the orthotopic MDA-MB-231 breast tumor-bearing nude mice ($n = 6$) were randomly grouped when the tumor volume reached ~100 mm^3. The tumor-bearing mice were intravenously injected with PBS, ARV771, PGDA nanoparticle or PGDAT nanoparticle with the identified ARV771 dose of 10 mg/kg and PPa dose of 5.0 mg/kg, respectively. The tumor sites of PGDA and PGDAT groups were irradiated with 671 nm laser (400 mW/cm^2) for 5 min at 36 h post nanoparticle injection. The treatment was repeated triplicate at a 3-day interval. The same experimental procedures were followed to investigate the antitumor activity of the ROS/hypoxia-activatable PROTAC nanoparticle in vivo, Both the tumor volume and the body weight of the mice were monitored throughout the experimental period. According to the animal ethics guidelines of the institute and animal welfare, the mice were considered death when the tumor volume exceeded 1500 mm^3. At the end of experiment, the major organs (heart, liver, spleen, lung and kidney) and tumor tissues of the mice were collected for H&E and TUNEL analysis. The tumor volume was calculated by formula below:

$$V = L \times W \times W/2 (L, \textit{the longest dimension}; W, \textit{the shortest dimension}).$$

Analysis of cancer stem-like cells in tumor tissue

The MDA-MB-231 tumor bearing-mice were randomly grouped ($n = 3$) once the tumor volume reached ~200 mm^3. The mice were treated with PBS, ARV771, PGDA nanoparticle, PGDAT nanoparticle or PGDAT@N nanoparticle at the identified ARV771 dose of 10 mg/kg and PPa dose of 5.0 mg/kg, respectively., the tumor sites of PGDA + laser, PGDAT + laser and PGDAT@N + laser groups were irradiated with 671 nm laser at photodensity of 400 mW/cm^2 for 5 min 36 h post-injection. The treatment was repeated for 3 cycles at a 3-day interval. Following treatment, the tumor tissues were collected, and digested with enzyme solution (collagenase IV, Hyaluronidase and DNase I) by using a tissue processor (Gentle MACS Dissociator, Militenyi Biotec GmbH, Germany). The single cell suspension was obtained by filtering through a 70 μm filter membrane, and further stained with fluorescence-labeled antibody according to the manufacturer's protocol prior to flow cytometric examination. To assess the ratio of cancer stem-like cell within the tumor tissue, the cells were stained with anti-CD44-APC antibody and anti-CD24-PerCP-Cy 5.5 antibody. To analysis the expression of stem-associated transcription factors in the tumor tissue, the obtained single cells were pretreated with BD Cytofix/Cytoperm™ fixation/permeabilization solution kit firstly, and then stained with anti-NANOG, anti-SOX2, anti-OCT4 antibodies respectively, further stained with Alexa Fluor 647-conjugated second antibody.

Laser irradiation-induced hypoxic tumor microenvironment

MDA-MB-231 tumor-bearing mice were intravenously injected PGDAT nanoparticle when the tumor volume reached ~150 mm^3. The tumor was treated with 671 nm laser irradiation (400 mW/cm^2, 5 min) 36 h post-injection. After an additional 12 h, the pimonidazole was intravenously injected into the mice following the protocol of Hypoxyprobe™ kit., the tumor tissues were collected 2 h post nanoparticle injection and section for CLSM examination.

RNA sequencing analysis

MDA-MB-231 cells and enriched MDA-MB-231 stem-like cells were treated with ARV771 at the concentration of 1 μM for 24 h, and then the cells were collected for total RNA extraction using TRIzol® Reagent. Genomic DNA was removed by DNase I, and the 1% agarose gels were used to monitor the RNA degradation and contamination. Next, RNA quality was identified by 2100 Bioanalyser (Agilent Technologies) and quantified by ND-2000 (NanoDrop Technologies). RNA sample with high-quality was utilized to establish sequencing library (OD260/280 = 1.8 ~ 2.2, OD260/230 ≥ 2.0, RIN ≥ 8.0, 28 S:18 S ≥ 1.0 and ≥ 1 μg).

RNA purification, reverse transcription, library establishment and sequencing were completed at Shanghai Major Bio-pharm Biotechnology Co., Ltd. (Shanghai, China). Briefly, the transcriptome library was constructed according to the TruSeq™ RNA sample preparation Kit from Illumina (San Diego, CA) with 1 μg of total RNA. To analysis differential expression genes (DEGs) between different samples, the expression level of each gene was calculated according to the transcripts per million reads (TPM). For identifying differentially expressed genes, a suite of analytical tools including DESeq2/DEGseq/edgeR/Limma/NOIseq, DEGs with $|\log2(\text{foldchange})| \geq 1$ and P-adjust ≤ 0.05 (DESeq2/edgeR/Limma) / P-adjust ≤ 0.001 (DEGseq) / Prob > 0.8 (NOIseq), indicating significant differential expression. Besides, functional-enrichment analysis of Kyoto Encyclopedia of Genes and Genomes (KEGG, http://www.genome.jp/kegg/) was performed to identify which DEGs were significantly enriched in metabolic pathways with P-adjust ≤ 0.05 compared to the whole-transcriptome background. KEGG pathway analysis were carried out by KOBAS.

Gene transcription determined by real-time PCR

MDA-MB-231 cells and MDA-MB-231 stem-like cells were incubated with predetermined ARV771, ARV771 derivates or PROTAC nanoparticle with the identified ARV771 concentration of 1 μM for 24 h. Then, the cells were harvested and extracted the total RNA through TRIzol Reagent according to the manufacturer's protocol. Next, RNA was quantified by ND-2000 (NanoDrop Technologies). DNA removal was completed through PrimeScript™RT reagent Kit with gDNA Eraser according to the operating protocol. TB Green® Premix Ex Taq™ II was utilized for the PCR amplification and real-time PCR examination (Bio-Rad, CFX 96 Touch, USA). The primers used in this work are provided in Supplementary Table 2.

Inhibition of tumor spheroids formation

MDA-MB-231 tumor cells were incubated with ARV771 or ARV771 derivates in the 6-well ultralow attachment plates, cultured in the CSCs medium for 12 days to form the tumor spheroids (counted at diameter > 50 μm).

Region-confined prodrug activation in tumor tissue

When the MDA-MB-231 tumor volume reached ~150 mm^3, the mice were grouped as PBS, PGDAC + Laser, PGDAC@N and PGDAC@N + Laser., The mice assigned to laser-treated group were subjected to 671 nm laser irradiation (400 mW/cm^2, 5 min) 36 h post intravenously injection of the nanoparticle. Both mice were intravenously injected with pimonidazole (60 mg/kg) 1.5 hours prior to the laser irradiation. Then 0.5 h post-laser irradiation, the tumor tissues were collected and sectioned for CLSM examination ex-vivo.

Antitumor study in HN30 xenograft tumor model in vivo

The xenograft HN30 human head and neck carcinoma tumor model was further used to evaluate the antitumor performance of ROS/hypoxia-activatable PROTAC nanoparticle in vivo. For establishing HN30 tumor model, 100 μL of cell suspension (5.0×10^6 cells) was subcutaneously injected into the back of BALB/c nude mice. The tumor bearing-mice were randomly grouped ($n = 6$) when the tumor volume reached ~100 mm^3, and i.v. injected with PBS, PGDAT nanoparticle or PGDAT@N nanoparticle. Upon 36 h post nanoparticle injection, the tumor of PGDAT and PGDAT@N groups were treated with 671 nm laser for 5 min at a photo-density of 400 mW/cm^2 for 3 cycles. The tumor volume and body weight of the animals was monitored throughout the experimental period. According to the animal ethics guidelines of our institute and animal welfare, the mice were considered death when the tumor volume exceeded 1500 mm^3. The tumor tissues of the mice were collected for H&E and TUNEL analysis at the end of antitumor studies.

Statistics and reproducibility

All data were presented as mean ± SD. Statistical analysis was performed using GraphPad Prism software 8.2.1. Two-tailed Student's *t*-test and One-way analysis of variance (ANOVA) with a Tukey post hoc test were used for the statistical comparison between the two groups and among multiple groups, respectively. And survival study was analyzed through Two-sided log-rank (Mantel-Cox) test. No statistical method was used to predetermine sample size. No data were excluded from the analyses; The experiments were not randomized; The Investigators were not blinded to allocation during experiments and outcome assessment.

Reporting summary

Further information on research design is available in the Nature Portfolio Reporting Summary linked to this article.

Data availability

The authors declare that the data supporting the findings of this study are available within the article, source data, and its Supplementary Information. The source data are provided with this paper. The raw data generated for the RNA-seq analysis are available from the NCBI SRA database under the accession code PRJNA1099160. All the NMR related data are available in the source data. The mass spectrometry data are available in the Supplementary Information. A reporting summary for this article is available as a Supplementary Information file. Source data are provided with this paper.

References

1. Schapira, M., Calabrese, M. F., Bullock, A. N. & Crews, C. M. Targeted protein degradation: expanding the toolbox. *Nat. Rev. Drug Discov.* **18**, 949–963 (2019).
2. Dale, B. et al. Advancing targeted protein degradation for cancer therapy. *Nat. Rev. Cancer* **21**, 638–654 (2021).
3. Li, K. & Crews, C. M. PROTACs: past, present and future. *Chem. Soc. Rev.* **51**, 5214–5236 (2022).
4. Sakamoto, K. M. et al. Protacs: chimeric molecules that target proteins to the Skp1-Cullin-F box complex for ubiquitination and degradation. *Proc. Natl Acad. Sci. USA* **98**, 8554–8559 (2001).
5. Winter, G. E. et al. Phthalimide conjugation as a strategy for in vivo target protein degradation. *Science* **348**, 1376–1381 (2015).
6. Burslem, G. M. & Crews, C. M. Proteolysis-Targeting Chimeras as Therapeutics and Tools for Biological Discovery. *Cell* **181**, 102–114 (2020).
7. Sosič, I., Bricelj, A. & Steinebach, C. E3 ligase ligand chemistries: from building blocks to protein degraders. *Chem. Soc. Rev.* **51**, 3487–3534 (2022).
8. Popovic, D., Vucic, D. & Dikic, I. Ubiquitination in disease pathogenesis and treatment. *Nat. Med.* **20**, 1242–1253 (2014).
9. Ming, H. et al. Protein degradation: expanding the toolbox to restrain cancer drug resistance. *J. Hematol. Oncol.* **16**, 6 (2023).
10. Békés, M., Langley, D. R. & Crews, C. M. PROTAC targeted protein degraders: the past is prologue. *Nat. Rev. Drug Discov.* **21**, 181–200 (2022).
11. Raina, K. et al. PROTAC-induced BET protein degradation as a therapy for castration-resistant prostate cancer. *Proc. Natl Acad. Sci. USA* **113**, 7124–7129 (2016).
12. Moreau, K. et al. Proteolysis-targeting chimeras in drug development: A safety perspective. *Br. J. Pharmacol.* **177**, 1709–1718 (2020).
13. Maneiro, M. A. et al. Antibody-PROTAC Conjugates Enable HER2-Dependent Targeted Protein Degradation of BRD4. *ACS Chem. Biol.* **15**, 1306–1312 (2020).
14. Liu, J. et al. Cancer Selective Target Degradation by Folate-Caged PROTACs. *J. Am. Chem. Soc.* **143**, 7380–7387 (2021).
15. He, S. et al. Aptamer-PROTAC Conjugates (APCs) for Tumor-Specific Targeting in Breast Cancer. *Angew. Chem. Int. Ed. Engl.* **60**, 23299–23305 (2021).
16. Liu, J. et al. Light-induced control of protein destruction by opto-PROTAC. *Sci. Adv.* **6**, eaay5154 (2020).
17. Xue, G., Wang, K., Zhou, D., Zhong, H. & Pan, Z. Light-Induced Protein Degradation with Photocaged PROTACs. *J. Am. Chem. Soc.* **141**, 18370–18374 (2019).
18. Reynders, M. et al. PHOTACs enable optical control of protein degradation. *Sci. Adv.* **6**, eaay5064 (2020).
19. Yang, C., Yang, Y., Li, Y., Ni, Q. & Li, J. Radiotherapy-Triggered Proteolysis Targeting Chimera Prodrug Activation in Tumors. *J. Am. Chem. Soc.* **145**, 385–391 (2023).
20. Shi, S. et al. Rational Design for Nitroreductase (NTR)-Responsive Proteolysis Targeting Chimeras (PROTACs) Selectively Targeting Tumor Tissues. *J. Med. Chem.* **65**, 5057–5071 (2022).
21. Liang, C. et al. Enzyme-Catalyzed Activation of Pro-PROTAC for Cell-Selective Protein Degradation, CCS. *Chemistry* **4**, 3809–3819 (2022).
22. Yang, T. et al. A BRD4 PROTAC nanodrug for glioma therapy via the intervention of tumor cells proliferation, apoptosis and M2 macrophages polarization. *Acta Pharm. Sin. B* **12**, 2658–2671 (2022).
23. Gao, J. et al. Engineered bioorthogonal POLY-PROTAC nanoparticles for tumour-specific protein degradation and precise cancer therapy. *Nat. Commun.* **13**, 4318 (2022).
24. Zou, Z. et al. Tumor-targeted PROTAC prodrug nanoplatform enables precise protein degradation and combination cancer therapy. *Acta Pharmacol. Sin.* https://doi.org/10.1038/s41401-024-01266-z (2024).
25. Meacham, C. E. & Morrison, S. J. Tumour heterogeneity and cancer cell plasticity. *Nature* **501**, 328–337 (2013).
26. Dagogo-Jack, I. & Shaw, A. T. Tumour heterogeneity and resistance to cancer therapies. *Nat. Rev. Clin. Oncol.* **15**, 81–94 (2018).
27. Shackleton, M., Quintana, E., Fearon, E. R. & Morrison, S. J. Heterogeneity in cancer: cancer stem cells versus clonal evolution. *Cell* **138**, 822–829 (2009).
28. Shibue, T. & Weinberg, R. A. EMT, CSCs, and drug resistance: the mechanistic link and clinical implications. *Nat. Rev. Clin. Oncol.* **14**, 611–629 (2017).
29. Baumann, M., Krause, M. & Hill, R. Exploring the role of cancer stem cells in radioresistance. *Nat. Rev. Cancer* **8**, 545–554 (2008).
30. Reya, T., Morrison, S. J., Clarke, M. F. & Weissman, I. L. Stem cells, cancer, and cancer stem cells. *Nature* **414**, 105–111 (2001).
31. Shen, S. et al. A nanotherapeutic strategy to overcome chemotherapeutic resistance of cancer stem-like cells. *Nat. Nanotechnol.* **16**, 104–113 (2021).
32. Pützer, B. M., Solanki, M. & Herchenröder, O. Advances in cancer stem cell targeting: How to strike the evil at its root. *Adv. Drug Deliv. Rev.* **120**, 89–107 (2017).

33. Diehn, M. et al. Association of reactive oxygen species levels and radioresistance in cancer stem cells. *Nature* **458**, 780–783 (2009).
34. Zhang, J. & Li, L. Stem cell niche: microenvironment and beyond. *J. Biol. Chem.* **283**, 9499–9503 (2008).
35. Li, Z. & Rich, J. N. Hypoxia and hypoxia inducible factors in cancer stem cell maintenance. *Curr. Top. Microbiol. Immunol.* **345**, 21–30 (2010).
36. Kim, J. H. et al. A Small Molecule Strategy for Targeting Cancer Stem Cells in Hypoxic Microenvironments and Preventing Tumorigenesis. *J. Am. Chem. Soc.* **143**, 14115–14124 (2021).
37. Bai, L. et al. Targeted Degradation of BET Proteins in Triple-Negative Breast Cancer. *Cancer Res.* **77**, 2476–2487 (2017).
38. Zhou, F. et al. Engineering Chameleon Prodrug Nanovesicles to Increase Antigen Presentation and Inhibit PD-L1 Expression for Circumventing Immune Resistance of Cancer. *Adv. Mater.* **33**, e2102668 (2021).
39. Xu, J. et al. Dual stimuli-activatable versatile nanoplatform for photodynamic therapy and chemotherapy of triple-negative breast cancer. *Chin. Chem. Lett.* **34**, 108332 (2023).
40. Hou, B. et al. Engineering Stimuli-Activatable Boolean Logic Prodrug Nanoparticles for Combination Cancer Immunotherapy. *Adv. Mater.* **32**, e1907210 (2020).
41. Wang, D. et al. Acid-Activatable Versatile Micelleplexes for PD-L1 Blockade-Enhanced Cancer Photodynamic Immunotherapy. *Nano Lett.* **16**, 5503–5513 (2016).
42. Ye, J. et al. Bispecific Prodrug Nanoparticles Circumventing Multiple Immune Resistance Mechanisms for Promoting Cancer Immunotherapy. *Acta Pharma. Sin. B* **12**, 2695–2709 (2022).
43. Zhou, F. et al. Overcoming immune resistance by sequential prodrug nanovesicles for promoting chemoimmunotherapy of cancer. *Nano Today* **36**, 101025 (2021).
44. Zhou, F. et al. Tumor Microenvironment-Activatable Prodrug Vesicles for Nanoenabled Cancer Chemoimmunotherapy Combining Immunogenic Cell Death Induction and CD47 Blockade. *Adv. Mater.* **31**, e1805888 (2019).
45. Zhou, M. et al. Nanovesicles loaded with a TGF-β receptor 1 inhibitor overcome immune resistance to potentiate cancer immunotherapy. *Nat. Commun.* **14**, 3593 (2023).
46. Xu, J. et al. Dual stimuli-activatable versatile nanoplatform for photodynamic therapy and chemotherapy of triple-negative breast cancer. *Chin. Chem. Lett.* **12**, 108332 (2023).
47. Wan, Y., Fu, L. H., Li, C., Lin, J. & Huang, P. Conquering the Hypoxia Limitation for Photodynamic Therapy. *Adv. Mater.* **33**, e2103978 (2021).
48. Shen, S. et al. Combating Cancer Stem-Like Cell-Derived Resistance to Anticancer Protein by Liposome-Mediated Acclimatization Strategy. *Nano Lett.* **22**, 2419–2428 (2022).
49. Liu, M. et al. Hierarchical Nanoassemblies-Assisted Combinational Delivery of Cytotoxic Protein and Antibiotic for Cancer Treatment. *Nano Lett.* **18**, 2294–2303 (2018).
50. Dong, J. et al. Transcriptional super-enhancers control cancer stemness and metastasis genes in squamous cell carcinoma. *Nat. Commun.* **12**, 3974 (2021).
51. Cazares-Körner, C., Pires, I. M. & Hammond, E. M. CH-01 is a hypoxia-activated prodrug that sensitizes cells to hypoxia/reoxygenation through inhibition of Chk1 and Aurora A. *ACS Chem. Biol.* **8**, 1451–1459 (2013).
52. Zhou, S. et al. A Paclitaxel Prodrug Activatable by Irradiation in a Hypoxic Microenvironment. *Angew. Chem. Int. Ed.* **59**, 23198–23205 (2020).
53. Cheng, P. et al. Unimolecular Chemo-fluoro-luminescent Reporter for Crosstalk-Free Duplex Imaging of Hepatotoxicity. *J. Am. Chem. Soc.* **141**, 10581–10584 (2019).

Acknowledgements

This work was supported by the National Natural Science Foundation of China (U22A20328 to H.J.Y., 22074043 and 32311530041 to Z.A.X.), Science and Technology Commission of Shanghai Municipality (23ZR1475000 and 20430711800 to H.J.Y., 19DZ2251100 to H.X.X.), Shanghai Municipal Health Commission (SHSLCZDZK 03502 to H.X.X.), Scientific Research and Development Fund of Zhongshan Hospital of Fudan University (2022ZSQD07 to H.X.X.), The Mass Spectrometry System and the cell sorter BD Influx of the National Facility for Protein Science in Shanghai (NFPS), Shanghai Advanced Research Institute, CAS are gratefully acknowledged. All animal procedures were carried out under the guidelines approved by the Institutional Animal Care and Use Committee (IACUC) of the Shanghai Institute of Materia Medica, CAS.

Author contributions

J.G., H.J.Y., Z.A.X. and H.X.X. conceived the project, J.G., H.J.Y. and Z.A.X. designed the study. J.G., X.Y.J., W.H.C., M.L., Y.L., L.Y., and S.M.L performed the experiments and prepared the manuscript. J.G., X.H.C., P.F.L., M.H., H.J.Y., Z.A.X. and H.X.X. revised the manuscript. All authors have approved the final version of the manuscript

Competing interests

The authors declare no competing interests.

Additional information

Supplementary information The online version contains supplementary material available at https://doi.org/10.1038/s41467-024-50735-w.

Correspondence and requests for materials should be addressed to Haijun Yu, Huixiong Xu or Zhiai Xu.

Peer review information *Nature Communications* thanks the anonymous, reviewer(s) for their contribution to the peer review of this work. A peer review file is available.